ULTRA LOW THERMAL CONDUCTIVITY IN LAYERED DISORDERED CRYSTALLINE MATERIALS

BY

CATALIN CHIRITESCU

DISSERTATION

Submitted in partial fulfillment of the requirements
for the degree of Doctor of Philosophy in Materials Science and Engineering
in the Graduate College of the
University of Illinois at Urbana-Champaign, 2010

Urbana, Illinois

Doctoral Committee:

Professor David G. Cahill, Chair
Professor Angus Rockett
Associate Professor Jian-Min Zuo
Associate Professor William P. King

ABSTRACT

This dissertation presents an alternative route to achieve ultralow thermal conductivity in a dense solid. Thin films of disordered layered crystalline materials were deposited using Modulated Elemental Reactants (MER) method. Cross-plane thermal conductivity was measured using Time-Domain Thermo Reflectance (TDTR) method; elastic properties were investigated using picosecond acoustics. The results are applied to reducing the thermal conductivity in misfit layer materials and multilayers containing disordered layered crystalline materials.

The cross-plane thermal conductivity of thin films of WSe_2 is as small as 0.05 W m^{-1} K^{-1} at room temperature, 30 times smaller than the *c*-axis thermal conductivity of single-crystal WSe_2 and a factor of 6 smaller than the predicted minimum thermal conductivity for this material. The ultralow thermal conductivity is attributed to the anisotropic bonding of the layered WSe_2 and orientational disorder in the stacking of well-crystallized WSe_2 sheets along the direction perpendicular to the surface. Disordering of the layered structure by ion bombardment increases the thermal conductivity.

I measured the room-temperature, cross-plane thermal conductivities and longitudinal speeds of sound of misfit-layer dichalcogenide films $[(PbSe)_m (TSe_2)_n]_i$ (T = W or Mo, m = 1-5, n = 1-5) synthesized by the MER. The thermal conductivities of these nanoscale layered materials are 5-6 times lower than the predicted minimum thermal conductivity Λ_{min} of PbSe. Thermal conductivity decreases with increasing content of the main source of anisotropy in the sample, the layered chalcogenide, and it is largely unaffected by variations in superlattice period.

I investigated the lower limit to the lattice thermal conductivity of Bi_2Te_3 and related materials using thin films synthesized by MER. The thermal conductivities of single layer films of Bi_2Te_3 , Bi_2Te_3 and Sb-doped Bi_2Te_3 and multilayer films of $(Bi_2Te_3)_m(TiTe_2)_n$ and $[(Bi_xSb_{1-x})_2Te_3]_m(TiTe_2)_n$ are measured by TDTR; the thermal conductivity data are compared to a Debye-Callaway model of heat transport by acoustic phonons. The homogeneous nanocrystalline films have average grains sizes $30 < d < 100$ nm as measured by the width of the (003) x-ray diffraction peak. Multilayer films incorporating turbostratic $TiTe_2$ enable studies of the effective thermal conductivity of Bi_2Te_3 layers as thin as 2 nm. In the limit of small grain size or layer thickness, the thermal conductivity of Bi_2Te_3 approaches the predicted minimum thermal conductivity of 0.31 W m^{-1} K^{-1}. The dependence of the thermal conductivity on grain size is in good agreement with the Debye-Callaway model. The use of alloy $(Bi,Sb)_2Te_3$ layers further reduces the thermal conductivity of the nanoscale layers to as low as 0.20 W m^{-1} K^{-1}.

ACKNOWLEDGMENTS

First and foremost, my thanks and appreciation go to my advisor, David Cahill. In all our years of scientific interactions I developed a new and improved research style. He is a larger-than-life example of what a scientist should be - in knowledge and in critical thinking; he lights the path for the students so our searches can be fruitful, yet throws no shadow to stifle creativity. Thank you, David.

The samples for this thesis and many wonderful discussions came from the Oregon team: David Johnson, Nguyen Ngoc, Clay Mortensen, Colby Heideman, Qiyin Lin, Mary Smeller. Thank you for the summer in your lab, the days and nights at Argonne, thank you for all the work and dedication along the years. I'll always be better for having met you.

I would like to thank the staff at Frederick Seitz Materials Research Laboratory for their assistance, especially Doug Jeffers, Mauro Sardela and Julio Soares. They made my life so much easier in countless occasions and saved me many hours of tedious measurements with helpful ideas and suggestions.

I would like to thank Robert Averback and See Wee Chee for their help in setting up and running the ion beam experiments. See Wee went above and beyond every time I needed his help and this acknowledgment is a small token of gratitude for his efforts.

Members of the Cahill group over the years: Shawn Putnam, Xuan Zheng, Zhenbin Ge, Xijing Zhang, Tamlin Matthews and of course, my office buddy Yee Kan Koh. The fun exchange of ideas and jokes made time go much faster and easier. So long, and thanks for all the fish!

I gratefully acknowledge the generous support of the Office of Naval Research. A special mention for DTEC Program Officer Mihal Gross for her dedication to the cause of thermoelectrics and ultralow thermal conductivity materials.

I enjoyed my time in Urbana-Champaign and Charleston in the company of friends: Linda and Greg, Bogdan and Cristina, Miha and Greg, Ilinca, Florin, Ileana and Alexandra, thank you for all the fun we had (and will have again)!

A special mention to Trudy Kriven and her team for getting my foot in the door at UIUC and for all her support. One day I'll have those gold “samples” for you, maybe enough to make a boomerang !

This thesis is dedicated to the most important people in my life: my wife Andreea and my son Alexandru - you are the treasures of my heart, thank you for all your love and support; my parents Corneliu and Eufrosina – you are my inspiration and my guidance, thank you for your unwavering faith in me; my brothers Dragos and Bogdan – I am proud to be your brother.

TABLE OF CONTENTS

LIST OF FIGURES

LIST OF ABBREVIATIONS

D-C	Debye-Callaway
DPA	Displacement Per Atom
EPMA	Electron Probe Micro Analysis
FWHM	Full Width at Half Maximum
MER	Modulated Elemental Reactants
RBS	Rutherford Backscattering Spectroscopy
SIMNRA	Simulation Program for the Analysis of NRA, RBS and ERDA
SRIM	Stopping and Range of Ions in Matter
TDTR	Time-domain Thermoreflectance
XRD	X-Ray Diffraction
XRR	X-Ray Reflectivity

LIST OF SYMBOLS

Λ	Thermal conductivity
Λ_{min}	Minimum thermal conductivity
λ	Laser wavelength
T	Temperature
v	Speed of sound
N	Number density of atoms
n	Index of refraction
h	Thickness
w_0	$1/e^2$ Radius of the laser beam
t	Delay time
V_{in}	In-phase component of the output signal of the rf lock-in amplifier
V_{out}	Out-phase component of the output signal of the rf lock-in amplifier
C	Volumetric heat capacity
G	Thermal conductance
ρ	Mass density
f	Modulation frequency of pump beam
R	Reflectivity coefficient

CHAPTER 1

INTRODUCTION

Thermal conductivity Λ is defined on a macroscopic scale as the ability of a material to conduct heat. Heat transfer at a microscopic scale is a diffusion process. In a solid material, thermal energy is transported by two types of carriers: charged particles (free electrons and/or holes) and the lattice vibrations (phonons). In an insulating polycrystalline solid, thermal transport is therefore mediated by phonons and a typical temperature dependence of thermal conductivity is depicted in Figure 1.

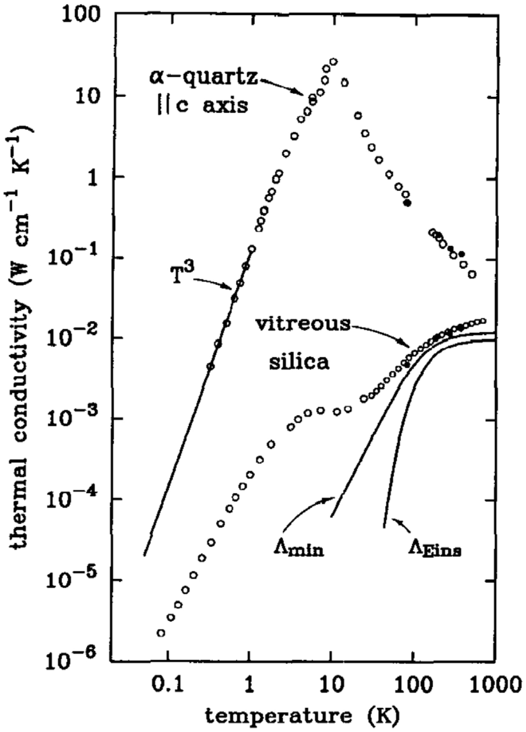

Figure 1. Temperature dependence of thermal conductivity for crystalline and amorphous materials. From D. G. Cahill and R. O. Pohl, Annu. Rev. Phys. Chem. 39, 93 (1988).

Thermal conductivity of crystals at low temperatures (T << Debye temperature) is dominated by boundaries scattering and it mirrors the behavior of specific heat and increases with temperature as Λ ~ T^3. At higher temperatures the phonons start interacting with each other in thermally resistive processes (i.e., umklapp scattering) and with defects in the crystal, causing the thermal conductivity to peak and then decrease as Λ ~ 1/T, with the numerical value of Λ depending upon the degree of anharmonicity of the material.2

The behavior depicted in Figure 1 can be described by the Klemens-Callaway (KC) model assuming a Debye density of states [1, 2]:

$$\Lambda = \frac{1}{2\pi^2 v}\left(\frac{k_B T}{\hbar}\right)^3 \int_0^{\frac{\Theta_D}{T}} x^2 \tau(x) C(x) dx , \tag{1}$$

where $x = \omega\hbar / k_B T$, with $\hbar$ and k_B denoting Planck's reduced and Boltzmann's constants, respectively, v is the speed of sound in the material, $\tau(x)$ is phonon relaxation time, $C(x)$ is the phonon specific heat, and θ_D is the Debye temperature. The central assumption of the KC model is that all phonon scattering processes are independent of each other and can be represented simply by a characteristic relaxation time τ.

In amorphous materials energy transfer by crystalline lattice waves is replaced by a random walk of vibrational energy between localized quantum oscillators [3]. Thermal conductivity in amorphous materials is reduced compared to that of crystalline materials (see Figure 1) and it typically increases with temperature, which is attributed to the increase of the heat capacity with temperature and the fact that the effective phonon mean-free path is weakly temperature dependent and mainly determined by structural disorder. In fact, an assumption that the mean-free-path is half the wavelength of the oscillators leads to the minimum thermal conductivity limit [4]:

$$\Lambda_{\min imum} = \left(\frac{\pi}{6}\right)^{\frac{1}{3}} k_B n^{\frac{2}{3}} \sum v_i \left(\frac{T}{\Theta_i}\right) \int_0^{\frac{\Theta_i}{T}} \frac{x^3 e^x}{e^x - 1} dx \,, \tag{2}$$

The unknowns in Equation 2 are the speeds v_i for the two longitudinal and one transversal sound modes and the number density of atoms n.

Recent studies have shown that the low limit of thermal conductivity in amorphous materials can be circumvented in multilayer crystalline thin films of metals and oxides [5, 6] with high interface density. This phenomenon is attributed to thermal resistance of the interfaces [7] (Kapitza resistance) which arises from differences in elastic properties and densities of vibrational states between materials on each side. When the spacing between the metal / oxide interfaces is of the order of mean free path of the phonons (a few nanometers) thermal conductivity of the multilayer circumvents the minimum thermal conductivity limit. In particular, when the interface density reaches 0.5 – 1 nm, the thermal conductivity of W/Al_2O_3 nanolaminates 5 is 3 times smaller than the thermal conductivity of amorphous Al_2O_3.

The objective of this dissertation is to present an alternative route to lower the thermal conductivity even farther below the minimum thermal conductivity limit using layered crystalline materials. My work has concentrated on metal dichalcogenide MX_2 layered materials. The structure of these materials consists of X-M-X tri-layer sheets with strong intra-layer bonding held together by weak Van der Waals forces. When prepared by alternating elemental layers of M and X and annealed, the resulting structure is disordered into small crystalline domains randomly stacked parallel with each other and with the deposition substrate. I used time-domain thermoreflectance to measure thermal conductivities as low as 0.05 W m^{-1} K^{-1} in thin films of tungsten diselenide, 6 times smaller than the predicted minimum thermal conductivity for this material and only a factor of 2 larger than the thermal conductivity of air.

The organization of this dissertation is as follows. Chapter 2 covers background information about the materials synthesis, and thermal and elastic properties measurement methods. Chapter 3 describes a study of the structure and thermal properties of disordered layered metal dichalcogenides. Chapter 4 reports thermal properties of misfit layer structures incorporating disordered layered materials. Chapter 5 investigates the lower limit to the lattice thermal conductivity of Bi_2Te_3 and related materials and compares the results with a Debye-Callaway model of heat transport by acoustic phonons.

CHAPTER 2

EXPERIMENTAL METHODS

2.1 Introduction

I measured the thermal conductivity of the samples discussed in this dissertation using the time-domain thermoreflectance (TDTR) [8, 9] method, as implemented by Cahill and coworkers [10, 11, 12]. TDTR is an ultrafast optical pump probe technique well suited for thermal metrology of thin films. On the time scale of the measurements (pico- to nanoseconds) the heat diffusion lengths in most materials is on the order of tens to hundreds of nanometers, thus enabling the user to resolve the thermal conductivity of the thin film and the thermal conductance of the film/substrate interface .

The samples discussed in Chapters 3-5 were deposited using the Modulated Elemental Reactants (MER) method [13, 14, 15]. In this process, thin films consisting of alternate layers of homogenous elemental constituents are transformed into an amorphous alloy during a solid-state reaction at low temperatures. The drive for this reaction is the large negative heat of mixing of the constituent elements so that the amorphous alloy product has a lower free energy than the two-phase multilayer reactant [16]. The amorphous alloy is then crystallized by heat treatment at higher temperatures. This technique allows the formation of materials otherwise hard to obtain (e.g., misfit layer compounds [17]).

The family of layered materials contains over 100 compounds listed in the literature [18, 19]. The family includes pure elements (such as C, P, As, Sb, Bi), binary and ternary inorganic compounds, organic compounds and silicates. Generally, the structure of these materials consists of a "sandwich" of strongly bonded sheets (covalent-ionic bonds) held together by weak Van der Waals forces. Electrically they cover a wide spectrum of properties, from semiconductors (WSe_2, $MoSe_2$, HfS_2) to semi-metallic ($TiSe_2$) and metallic behavior ($NbSe_2$, TaS_2). Due to their structural anisotropy the elastic properties and thermal conductivity in cross-plane direction are smaller compared to the in-plane ones (e.g., graphite: in-plane $\Lambda = 2000$ W m^{-1} K^{-1}, $C_{11} = 1440$ GPa, cross-plane $\Lambda = 8$ W m^{-1} K^{-1}, $C_{33} = 37$ GPa).

2.2 Modulated Elemental Reactants Method

In Modulated Elemental Reactants (MER) method the samples are prepared by sequentially depositing bilayers of the elemental components. In each bilayer, the ratio of the layer thicknesses is adjusted to obtain the composition corresponding to the stoichiometry of the desired component compound, and the absolute thickness of each bilayer is adjusted to provide the number of atoms required to form either a rock salt bilayer (PbSe), a dichalcogenide trilayer (WSe_2, $MoSe_2$, $NbSe_2$ or $TiTe_2$) or the five-layer structure of a unit cell of Bi_2Te_3 or Sb_2Te_3.

The elemental components are thermally evaporated in a high vacuum chamber [20] evacuated to 10^{-7} Torr and deposited onto as-received p-type Si (100) substrates (for TDTR and structure determination measurements) or polished fused silica slides (for electrical measurements) from SUMCO Sumitomo (0.01-0.02 Ω cm resistivity range). Bismuth (Bi), antimony (Sb), titanium (Ti), selenium (Se) and tellurium (Te) (99.995% purity) were acquired from Alfa Aesar. Lead (Pb), tungsten (W), niobium (Nb) and molybdenum (Mo) (99.95% purity) were acquired from PureTech Inc.

Bi, Sb, Se and Te were deposited using Veeco Applied Epi SUMO effusion cells with boron nitride crucibles. For Se, Te and Sb a boron nitride lid with a small hole was placed in the top of the crucible to improve the uniformity of the evaporated flux, by narrowing the deposition profile. The temperature of the tip and the base of the effusion cell were independently controlled with separate PID controllers. The tip was heated 150°C higher than the base to prevent condensation of the element being deposited. Tellurium was deposited with a tip temperature of 500°C at a rate of 1.0 Å/second. Selenium was deposited with a tip temperature of 350°C at a rate of 0.5 Å/second. Bi and Sb were deposited by applying current to both heaters. For bismuth a tip temperature of 750°C and a base temperature of 600°C was used to achieve a measured rate of 1.0 Å/second. For antimony a tip temperature of 710°C and a base temperature of 550°C achieved a measured rate of 1.0 Å/second.

W, Nb, Mo, Pb and Ti were deposited using a 6 kV Thermionics Laboratory electron beam gun. Titanium was deposited at a rate of 1.0 Å/second. W, Nb and Mo were deposited at a rate of 0.2 Å/second. Lead was deposited at a rate of 0.4 Å/second.

The deposition rates were monitored using quartz crystal microbalances placed at 25 inches above the sources and connected to the power control feedback of the PID controllers and electron beam guns. Silicon substrates were placed at 30 inches above the evaporation sources. The deposition rates were calculated assuming 100% tooling factors and ignoring the height difference between the substrates and the quartz crystal monitors. Computer controlled pneumatic source shutters controlled the deposition time and sequence of the elements.

Post deposition annealing is typically done in a dry nitrogen environment (<0.4 ppm O_2). The annealing schedule is described in detail in chapters 3-5.

Sample composition during thickness calibration was determined by electron-probe micro-analysis (EPMA) [21] using a Cameca SX-50 electron microprobe operating at 20 nA current, 1 μm spot size, and 8, 12 and 16 kV beam energies at multiple locations on the sample. The data are refined using the STRATAGem [22] software.

I used Rutherford backscattering spectroscopy (RBS) [23] (2 MeV He^{2+} ions, 150 degrees scattering angle and detector resolution 15 keV) to determine the areal density ρ_{RBS} (units of atoms cm^{-2}) of individual chemical elements in the samples prior to thermal conductivity measurements. RBS allows the quantitative determination of the composition of a material and depth profiling of individual elements without the need for reference samples, has a good depth resolution of the order of several nm, and a very good sensitivity for heavy elements of the order of parts-per-million (ppm). The accuracy of determining absolute atomic areal densities with the RBS method is 1% due to uncertainties in charge collection of the incident beam and the detector solid angle.

Data from RBS measurements is analyzed using SIMNRA software package [24]. An example of measurement for a standard 100 nm a-SiO_2 film grown on Si (100) substrate is shown in Figure 2. The conversion factors used to convert channel to energy in Figure 2 are calibration offset 131 keV and energy per channel 1.86 eV/ch.

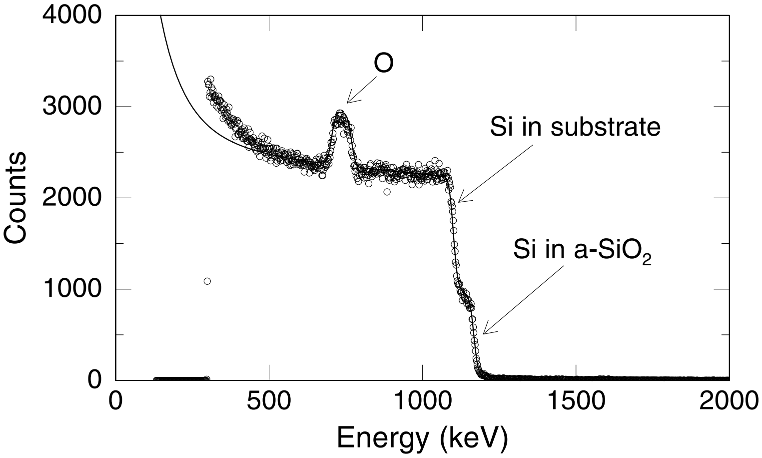

Figure 2. RBS spectra (open circles) and the SIMNRA fit (uninterrupted line) for 100 nm a-SiO$_2$ thermally grown on the Si substrate. Measured areal density is 650x10^{15} atoms cm^{-2}.

The areal density of a chemical element *i* in a thin layer is ρ_{RBS} (i) ~ A_i / σ_i , where A_i is the area under peak corresponding to element *i* in that layer after subtracting the background signal and σ_i is the scattering cross-section of the element *i* for 2 MeV He^{2+} ions [25]. For a thick layer, A_i is replaced by H_i, the signal height from the element *i* in the backscattering spectrum. It follows that for a layer of X_mY_n compound material the ratio of areal densities yields the stoichiometry of the respective layer $x = A_X \sigma_Y / A_Y \sigma_X$. I ignored the errors in scattering cross-sections and I estimated the accuracy of measuring the stoichiometry $\Delta x / x$ = 1.4% by calculating the square-root of the sum of squares of errors propagated from uncertainty in measurements of peak areas A_i (~ 1%).

Number density of atoms N can be determined from areal density using the relation N = ρ_{RBS} / h, where h is the thickness of the layer (typically measured by XRR). I compare values of N and absolute atomic ratios determined from RBS analysis with those estimated from the crystalline unit-cell parameters for the respective material: N = N_{atoms} x $N_{formulae}$ / $V_{unit\text{-}cell}$, where N_{atoms} and $N_{formulae}$ are the number of atoms and respectively , the number of formulae per unit-cell, $V_{unit\text{-}cell}$ is the volume of the unit cell. Mass density of a layer estimated from areal density measured by RBS is $\rho = \rho_{RBS} \times M_W / N_A / N_{atoms} / h$, where M_W is the molecular weight and N_A is the Avogadro's constant.

2.3 Time-Domain Thermoreflectance

2.3.1 Experimental Setup

In TDTR method a modulated pump beam is used to raise the temperature near the surface of the sample; the differences in reflected probe intensity caused by the heating due to the pump pulses are extracted with an rf lock-in amplifier synchronized to the modulation frequency of the pump. The output of the lock-in amplifier V has an in-phase component $V_{in}(t)$ and an out-of-phase component $V_{out}(t)$, $V(t) = V_{in}(t)+i\ V_{out}(t)$, where *t* is the delay time between the pump and probe beams. I compare the temporal evolution of the $V_{in}(t) / V_{out}(t)$ ratio with the predictions of a thermal model to obtain the thermal transport properties of the sample.

A schematic of the setup is presented in Figure 3. A mode-locked Ti:sapphire laser (1.5 W power, FWHM ~ 10 nm, λ = 710 - 900 nm tunable, vertical polarization, pulses with 0.1 ps duration at a rate of 80 MHz) is pumped by a CW solid state laser (10 W and λ = 532 nm). The wavelength and full width at half maximum (FWHM) of the Ti:sapphire laser are monitored by a spectrum analyzer; typically λ = 770 nm and FWHM = 10 nm. The output of the Ti:sapphire laser passes through the first $\lambda/2$ plate which acts as a power control, and then an optical isolator (to prevent unwanted back reflections). A convex lens with focal length of 2 meters collimates the laser beam which is then split into a pump and a probe beam using a polarized beam splitter (PBS) cube. The respective power ratio of the two beams is controlled by the PBS and a second λ/2 plate (typically 50-50 ratio).

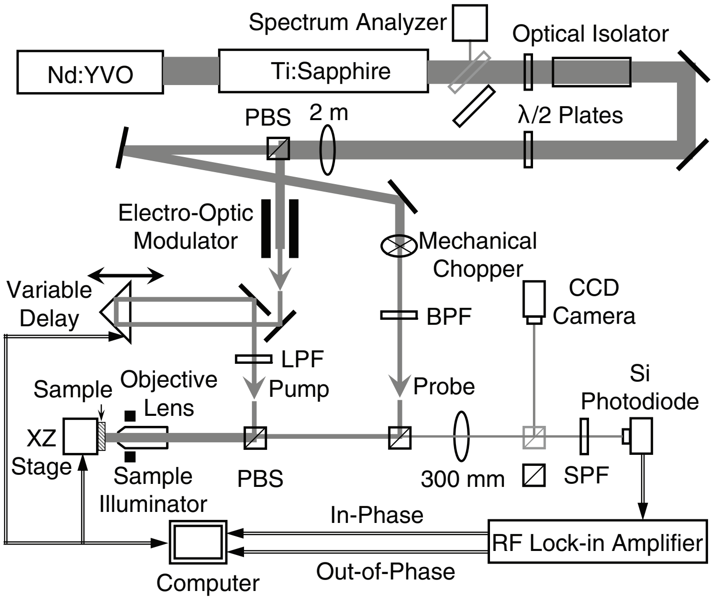

Figure 3. Schematic diagram of the TDTR experimental apparatus.

The intensity of the pump beam is modulated by an electro-optic modulator at frequency f (typically, f = 9.8 MHz). A difference in path length is introduced between the pump and probe beams using a computer-controlled mechanical stage, 500 mm in length (which translates into a time delay of ~ 4 ns). The vertically polarized pump beam is deflected by a second PBS before entering the objective lens. The probe beam is horizontally polarized after the split and is reflected by a non-polarizing beam splitter (BS) before entering the same objective lens. The pump and probe beam paths are parallel and separated vertically by 4 mm at the back focal plane of the objective lens.

To focus the beams on the sample accurately, a darkfield image is created in a CCD camera using an illumination ring and inserting a beam splitter into the beam path to deflect the light into the CCD. The pump and probe beams are focused in the same spot on the surface of the sample. I determined the $1/e^2$ radius of the laser spot size w_0 by analyzing the dependence of the in-phase signal on the overlap of the pump and probe beams. I overlapped the beams by steering the pump beam with the PBS via a high precision optical mount and two differential micrometers to maximize the amplitude of the photodetector output. In the present configuration, a micrometer motion of 1 micron deflects the pump beam by an angle of $\Delta\theta_x = 35$ μrad horizontally and $\Delta\theta_y = 24$ μrad vertically. The corresponding lateral displacements at the front focal plane of the objective lens with focal length F are $x = F\ \Delta\theta_x$ and $y = F\ \Delta\theta_y$, respectively. I assumed an overlap of two identical Gaussian beams and fitting the curves $V_{in}(x)$ and $V_{in}(y)$, I estimated $w_0 = 7.5$ μm for F = 20 mm (10 X objective), $w_0 = 15$ μm for F = 40 mm (5 X objective) and $w_0 = 3.5$ μm for F = 10 mm (20 X objective).

The reflected probe beam is collimated by the objective lens and it is focused on a Si photodiode by a convex lens with a focal length of 300 mm. The output of the Si photodiode is connected to a rf lock-in amplifier locked to the modulation frequency of the pump beam f. A resonant circuit filters the odd harmonics of pump beam modulation in the output of the Si photodiode by an inductor placed in series between the reverse-biased capacitance of the photodiode and the 50 Ω input of the rf lock-in amplifier. The inductance is selected to maximize the response at modulation frequency f. For a typical f = 9.8 MHz, L = 15.6 μH and the quality factor of the resonance circuit $Q \approx 10$.

The PBS behind the objective lens blocks most of the reflected pump beam but a significant fraction still passes due to the finite extinction ratio of the PBS, birefringence in the sample or optics, and depolarized light scattering. To suppress this background signal, I employed two mechanisms:

1. Acoustic frequency modulation of the probe beam by a mechanical chopper (200 Hz audio frequency) followed by spatial filtering using an optical aperture (see Figure 3). The photodiode signal has then frequency components of f ± 200 Hz. The signal is demodulated by the rf lock-in amplifier down to 200 Hz. The in-phase and out-of-phase outputs of the lock-in are picked up by a pair of computer-based audio frequency lock-in amplifiers locked to the modulation frequency of the probe beam, 200 Hz.

2. Spectral separation of pump and probe beams using sharp edge optical filters ("two-tint" method [26]). The center output wavelength of the Ti : sapphire laser is adjusted to 785 nm. A long-wave pass optical filter (LPF) with a cutoff at 790 nm is placed in the pump beam path. A bandpass filter (BPF) (center wavelength of 785 nm and a bandwidth of 3 nm) is placed in the probe beam path. The BPF is tilted to maximize the signal on the photodiode detector and shift the center frequency of the probe beam to 781 nm; a tilt angle of 13° creates a wavelength shift of 5 nm. This procedure separates the peak wavelengths of the pump and probe intensities by ~10 nm. Diffuse pump light scattered from the sample is then suppressed by a factor of ~1000 using a short-wave pass optical filter (SPF) with a cutoff of 780 nm placed before the Si photodiode.

The "two-tint" method improves upon the double modulation approach and becomes important for samples with increased surface roughness (thermoreflectance signal < 70% of specular reflection).

A thin film of aluminum (50-100 nm thick) is deposited on the samples by dc magnetron sputtering prior to measurements. It acts as a transducer to absorb the energy from the laser pulses and it has optimal thermoreflectance properties in the range of laser wavelengths used in my experiments.

I measured thermal conductivity at temperatures down to 80K by placing the samples in a liquid nitrogen (LN_2) cooled cryostat evacuated to 10^{-7} Torr by a turbo pump. An XZ computer-controlled stage allows the sample to be translated for thermal conductivity mapping.

The current implementation of TDTR method (using the $V_{in}(t)$ / $V_{out}(t)$ ratio of thermoreflectance signals) is a more robust measurement than the traditional implementation (measuring in-phase signal alone): both in-phase and out-of-phase signals are changed by the same factor when defocusing the pump beam and by changes in the pump-probe overlap [11, 27, 28]. In addition, the extra information in the out-of-phase signal increases the sensitivity of the measurement to the thermal conductivity of the sample layer.

2.3.2 TDTR Model and Data Analysis

The TDTR model is a numerical calculation of heat flow in a multilayer structure [10]. The heat diffusion equation is solved in the frequency domain by assuming temperature and heat flow continuity across layer boundaries and a periodic source of power with a Gaussian distribution of intensity. The frequency domain responses are then assembled to calculate the ratio of thermoreflectance signals as a function of the time delay between the pump and probe. Details of the calculation are given in Reference 10.

I determine the thermal conductivity of a thin layer by comparing the measured $V_{in}(t)$ / $V_{out}(t)$ ratio to the calculations of the thermal model. An interface with thermal conductance G is modeled by a layer with small thermal conductivity Λ_G, thickness h_G, and volumetric heat capacity C_G , where $G = \Lambda_G / h_G$. For a three layer (Al / sample film / substrate) configuration, the model has several parameters: $1/e^2$ radius of the laser spot size w_0, the thermal conductance G of the Al/sample interface, the thickness, thermal conductivity and volumetric heat capacity of Al layer (h_{Al}, Λ_{Al}, C_{Al}), the thermal conductivity and volumetric heat capacity of substrate (Λ_{sub}, C_{sub}), and the thickness h, thermal conductivity Λ and volumetric heat capacity C of the sample layer

The procedure for measuring w_0 is described in the Experimental Setup section. I typically measured h_{Al} using picosecond acoustics. The thickness of sample layers was measured by x-ray reflectivity (XRR) [29] from the low angle ($2\theta < 10$ degrees) Kiessig fringes i.e., subsidiary maxima resulting from X-ray interference from the front and back of the films. Aluminum thermal conductivity is derived from Wiedemann-Franz law using 4-point probe measurements of the electrical resistivity at 300 K. I estimated thermal conductivity of Al films at lower temperatures from the values at 300 K assuming a constant residual resistivity [30]. The heat capacity of the Al layer [31], and heat capacity [32] and thermal conductivity [33] of the crystalline Si (c-Si) substrate (the typical substrate used for my samples) are taken from literature values. Temperature-dependent heat capacity of the homogenous sample layers is taken from literature values: amorphous SiO_2 (a-SiO_2) [34], Bi_2Te_3 [35], Sb_2Te_3 [36], $TiTe_2$ [37], WSe_2 [38], $MoSe_2$ [39], $NbSe_2$ [40], and PbSe [41]. Heat capacity of multilayer samples is a volume weighted average of the heat capacities of the individual components.

No experimental data exists for amorphous silicon (a-Si) in the range $80 < T < 300$ K. Literature calculations [42, 43, 44] predict a difference between specific heat of c-Si and a-Si, $\Delta C = -0.224 + 4.85T / 1685$ J mol^{-1} K^{-1} for the temperature range $80 < T < 300$ K. Using specific heat values of c-Si from Reference 32, this translates into percentage increase $\Delta C / C_{c\text{-}Si}$ from 0.07 % at 80 K to 3 % at 300K. Therefore I used the values from Reference 32 as data for specific heat of a-Si.

The free parameters of the model, thermal conductance G of the Al/sample interface and thermal conductivity Λ of the sample are adjusted in the model to fit the experimental data at different delay times ranges (see Figure 4) [45]. At long delay times ($t > 2$ ns), $V_{in}(t) / V_{out}(t)$ has a stronger dependence on G. At short-to-intermediate delay times, $0.1 < t < 0.5$ ns, $V_{in}(t) / V_{out}(t)$ has a strong dependence on Λ and is only weakly dependent on G.

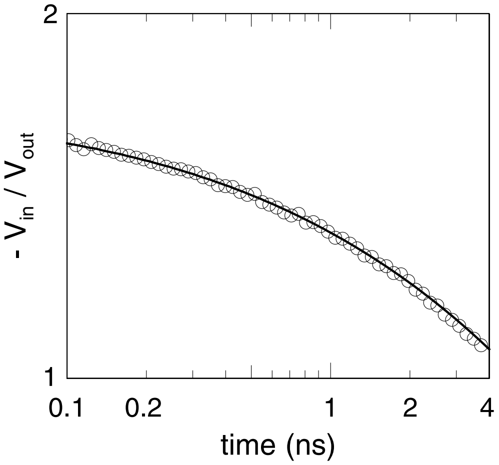

Figure 4. Ratio of the in-phase to out-of-phase voltage, $V_{in}(t) / V_{out}(t)$ (open circles) as a function of delay time t for a 1 μm thick film of amorphous SiO_2 (a-SiO_2) on Si substrate at 300K. The parameters for the model fit (uninterrupted line) are: f = 9.8 MHz, $w_0 = 7.5$ μm; $h_{Al} = 70.4$ nm, $\Lambda_{Al} = 196$ W m^{-1} K^{-1}, $C_{Al} = 2.44$ J cm^{-3} K^{-1}, a-SiO_2 C=1.64 J/cm^3-K; $\Lambda_{Si} = 142$ W m^{-1} K^{-1}, $C_{Si} = 1.64$ J cm^{-3} K^{-1}. The free parameters as a result of the fit are G = 200 MW/m^2-K and a-SiO_2 $\Lambda = 1.33$ W m^{-1} K^{-1}.

The TDTR method has been thoroughly validated by previous measurements on known materials [46]. To confirm the accuracy of my measurements, a standard sample of 1 micron thick amorphous SiO_2 thermally grown on Si was coated with Al and I measured it before every set of samples. The measured room temperature thermal conductivity (1.33 W m^{-1} K^{-1}) is within 2% of reference [47, 48] literature values (1.30 W m-1 K-1) for thermally grown SiO_2 and bulk a-SiO_2. The values at 88 K are within 8% of the same reference literature data, well within the error bars of the measurement.

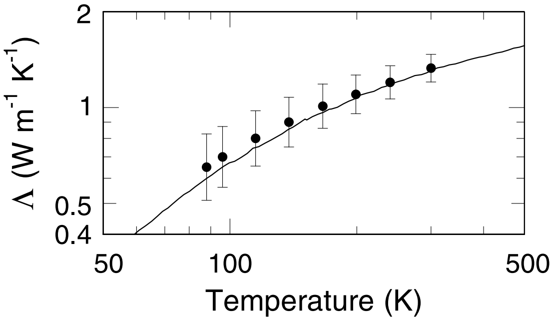

Figure 5. Temperature dependence of the thermal conductivity Λ (closed circles) for a 1 μm thick film of amorphous SiO_2 on Si substrate, measured with TDTR. For comparison reasons, I included the literature data from Reference 47 (continuous line).

2.3.3 Error Estimation and Corrections in TDTR Measurements.

I estimated the accuracy of measuring thermal conductivity of the sample Λ by calculating the square-root of the sum of the squares of errors propagated from uncertainty in measurements of each of the parameters of the model.

To gauge how a parameter influences the output of the model, a sensitivity factor S_α is defined [45] as:

$$S_\alpha = \frac{dln\left(-\frac{V_{in}}{V_{out}}\right)}{dln\alpha}, \qquad (3)$$

where α is any parameter of the thermal model. The error propagated from measurement uncertainty σ_α for a parameter α is then $\sigma_\alpha S_\alpha / S_\Lambda$, where S_Λ is the sensitivity factor for the thermal conductivity of the sample.

Figure 6 shows the variation of the sensitivity factors for different parameters as a function of film thickness for two typical samples in my study, an ultralow thermal conductivity sample (WSe_2 $\Lambda = 0.05$ W m^{-1} K^{-1}) and a higher thermal conductivity sample (Bi_2Te_3 $\Lambda = 0.8$ W m^{-1} K^{-1}).

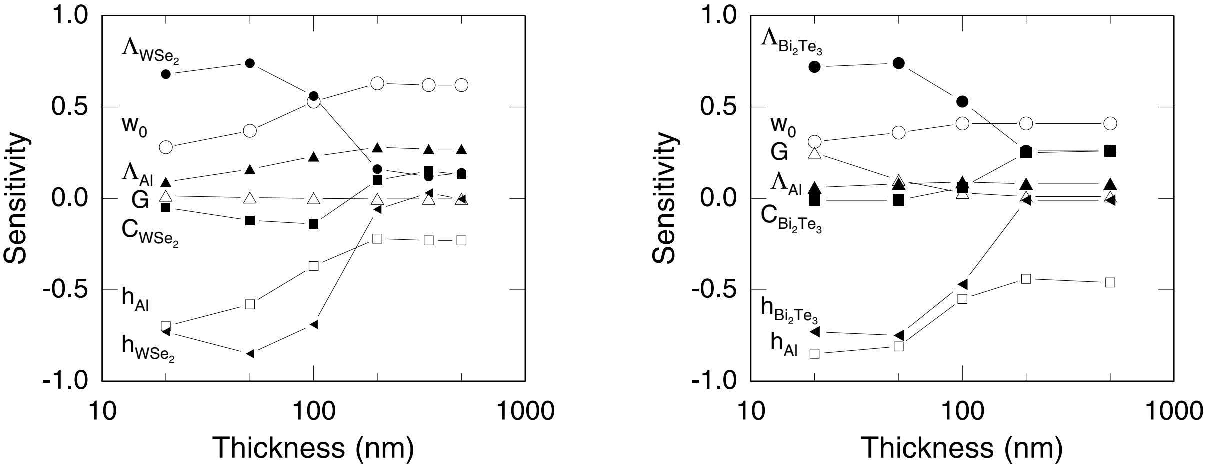

(A) **(B)**

Figure 6. Sensitivities to various parameters of the thermal model, plotted as function of the thickness for two thin film samples: (A) tungsten diselenide (WSe_2); (B) bismuth telluride (Bi_2Te_3). The parameters used in the calculations are: (A) pump beam modulation frequency 0.6 MHz, 1/e^2 radius of the laser spot w_0=14 microns; Al film, thickness 80 nm, thermal conductivity Λ=200 W m^{-1} K^{-1}, heat capacity C=2.44 J cm^{-3} K^{-1}; WSe_2 film, Λ=0.05 W m^{-1} K^{-1}, C=1.95 J cm^{-3} K^{-1}; Si substrate, Λ=142 W m^{-1} K^{-1}, C=1.64 J cm^{-3} K^{-1}; (B) pump beam modulation frequency 9.8 MHz, 1/e^2 radius of the laser spot w_0=7.5 microns; Al film, thickness 77 nm, thermal conductivity Λ=200 W m^{-1} K^{-1}, heat capacity C=2.44 J cm^{-3} K^{-1}; Bi_2Te_3 film, Λ=0.75 W m^{-1} K^{-1}, C=1.24 J cm^{-3} K^{-1}; Si substrate, Λ=142 W m^{-1} K^{-1}, C=1.64 J cm^{-3} K^{-1}. The temperature is 300K and sensitivity is calculated at 0.1 ns delay time

The sensitivity to thermal properties of the sample layer is largest when the thermal penetration depth l is larger than the film thickness; $l = (\Lambda/C/\omega)^{1/2}$, where D = Λ/C is the thermal diffusivity of the sample layer and $\omega = 2\pi f$ is the angular frequency of the modulation of the pump beam. As the thickness of sample layer increases, the sensitivity factor for thermal conductivity S_Λ drops. For thicker samples, the spot size w_0 also becomes more important.

The accuracy is dominated by uncertainties in measurements of the thickness h_{Al} and thermal conductivity Λ_{Al} of the Al film, thickness h of the sample, and the $1/e^2$ radius w_0 of the laser spot.

The accuracy in measuring h_{Al}, h and w_0 are each estimated at 5%. The accuracy for Λ_{Al} is estimated at 5% at 300 K and 15% at 80 K due to deviations from the Wiedemann-Franz law [49]. Overall accuracy in measuring Λ is shown as error bars in the figures in chapters 3-6 and range between 10% at 300 K and 25% at 88 K.

The precision of TDTR measurements is dominated by the phase difference between the thermoreflectance signal and the reference channel input to the rf lock-in amplifier. The difference is removed by adjusting the reference channel so that $V_{out}(t)$ is continuous when delay time crosses from negative to positive times, i.e., the thermoreflectance signal before and after the arrival of pump beam to the surface of the sample. The change in phase is $\varepsilon \approx \Delta V_{out}/V_{in}$, where ΔV_{out} is standard deviation of V_{out}. We correct the overall thermoreflectance signal $(V_{in} + i\, V_{out})$ by a factor of $(1 + i\, \varepsilon)$, which propagates into an error $\sigma = V_{in}\, \varepsilon / V_{out}$ in the ratio of thermoreflectance signals. The precision in measuring Λ is then $\sigma / S_\Lambda = \Delta V_{out} / V_{out} / S_\Lambda$ and is < 2% for the range of samples in my study.

The steady state temperature rise ΔT averaged over the size of the probe beam during the measurements is $\Delta T = I\,(1 - R) / (2\Lambda\, w_0 \sqrt{\pi})$, where I is the power of the pump and probe beams and R is the reflectivity of Al at the pump/probe beam wavelength (typically 13% at 770 nm). The fixed parameters of the model are adjusted to take into consideration this temperature rise.

2.3.4 Mapping of Thermal Conductivity Using TDTR

A map of thermal conductivity of can be realized by scanning the lateral cross-section of a sample, recording the thermoreflectance signal at a fixed delay time and then converting the V_{in} / V_{out} 2-D profile into a map of thermal conductivities. I run a spot TDTR measurement for the full range of delay times and then using a relation calculated from the thermal model I convert the map of V_{in} / V_{out} ratios to a map of effective thermal conductivities $\Lambda_{eff.} = \Lambda C / C_0$. Λ and C are the sample thermal conductivity and heat capacity at each spatial location and C_0 is the heat capacity at the spatial location used for thermal profile conversion.

For delay times in the range 100 ps < t < 500 ps, heat has diffused uniformly through the Al film but little heat has entered the sample because of the limited thermal conductance of the Al / sample interface. Thus, the in-phase thermoreflectance signal is proportional to E / (h_{Al} C_{Al}), where (h_{Al} C_{Al}) is the heat capacity per unit area of the Al film and E is the energy in each pump optical pulse. The out-of-phase thermoreflectance signal is proportional to the imaginary part of the frequency response at the modulation frequency of the pump beam. Since heat diffuses a distance in the sample that is large compared to the thickness of the Al film, the imaginary part of the frequency response is proportional to $P / (C \Lambda f)^{1/2}$, where $(C \Lambda)^{1/2}$ is the thermal effusivity of the sample, f is the modulation frequency of the pump beam, and P is the power of the pump beam. The ratio $V_{in}(t) / V_{out}(t)$ at short to intermediate delay times is therefore approximately proportional to $\Lambda^{1/2}$. I use a second degree polynomial to perform the conversion as described above. The lateral resolution of the measurement is mostly controlled by the laser spot size w_0. Because the thermoreflectance signal arises from the product of the pump and probe fluence, the effective spot size of the measurement is $w_0 / \sqrt{2}$.

The advantage of this method is that it enables a quick thermal profile of a section through a multilayer [50] or composition gradient [51] sample. However, the precision of thermal conductivity measurements at a single delay time is worse than measurements utilizing the full range of delay time because of larger uncertainties in the phase of the reference channel and uncertainties in the thermal conductance G of Al / sample interface.

2.3.5 Measurements of Elastic Properties

I used picosecond acoustics [52] and picosecond interferometry [53, 54] to measure the thickness of the Al film and cross-plane speed of sound in the samples of interest.

In picosecond acoustics, the Al film deposited on the sample partially absorbs the pump laser pulse and expands, generating an acoustic/strain pulse that propagates away from the surface of the sample. The acoustic pulse reflects from interfaces in the sample and returns to the surface of the Al film where it changes the local index of refraction and thus is detected by variations (positive or negative peaks) in the thermoreflectance signal. To determine the sign of the variation the following observation applies: an acoustic pulse will undergo a phase shift by π (or zero) when reflected from an interface with a layer with lower (or higher) acoustic impedance $Z = \rho v$, where ρ is the density and v is the longitudinal speed of sound in the said layer. If we write the acoustic impedances on either side of an interface as Z_2 and Z_1, the coefficient of reflection for normal incidence is $R = (Z_2 - Z_1) / (Z_2 + Z_1)$ and $-1 < R < 1$; the amplitude of the acoustic peaks in the thermoreflectance signal is influenced by the value of R and the absorption/transmission coefficient of the layers that the acoustic echo traverses when returning to the surface of Al layer.

The thickness of the Al film is calculated from the arrival time t for acoustic echoes from the Al / sample interface using the bulk longitudinal speed of sound [55] for Al $v_{Al} = 6.42$ nm/ps: $h_{Al} = v_{Al}\, t / 2$. A native aluminum oxide film approximately 3 nm thick forms on the Al layer after the deposition and its thickness is added to the value determined by acoustic echoes when inserted in the thermal model. The origin of time scale (i.e., $t = 0$) is the coincidence of the pump and probe beams and I use the location half way between the start and the maximum of the coincidence peak.

An example of measurement to determine the Al thickness is shown in Figure 7 and Figure 8. In Figure 7, acoustic impedance of glass [55] ($\rho = 2.5$ g cm^{-3}, $v_{glass} = 5.7$ nm ps^{-1}) is less then that of the Al layer55 ($\rho = 2.7$ g cm^{-3}, $v_{Al} = 6.42$ nm ps^{-1}). The strain wave undergoes a π phase change at Al/glass interface so the first echo peak is negative; after a second π phase change at Al/air interface, the strain wave is reflected off the Al / glass interface with another π phase change, therefore the second echo peak is also negative.

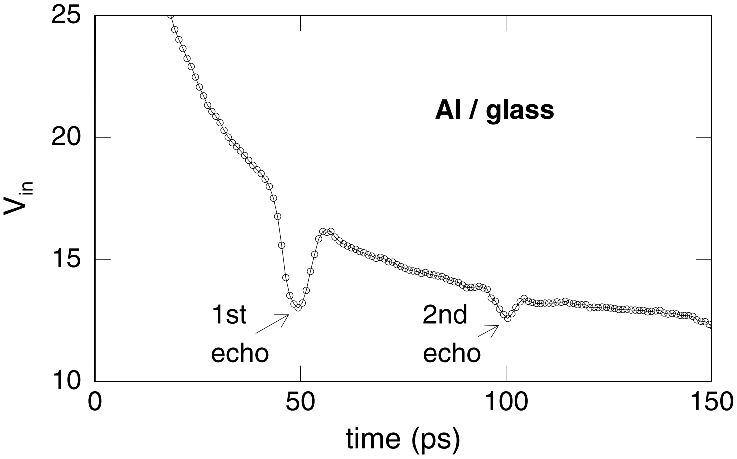

Figure 7. Picosecond acoustics measurements for an Al film deposited on soda-lime glass slide. Arrival time of echoes from the Al/glass interface are t_1 = 50 ps and t_2 = 100 ps. Al layer thickness estimated from this measurement is $h_{Al} = v_{Al} (t_2 - t_1) / 2$ = 160.5 nm. Measurement was performed at f = 9.8 MHz.

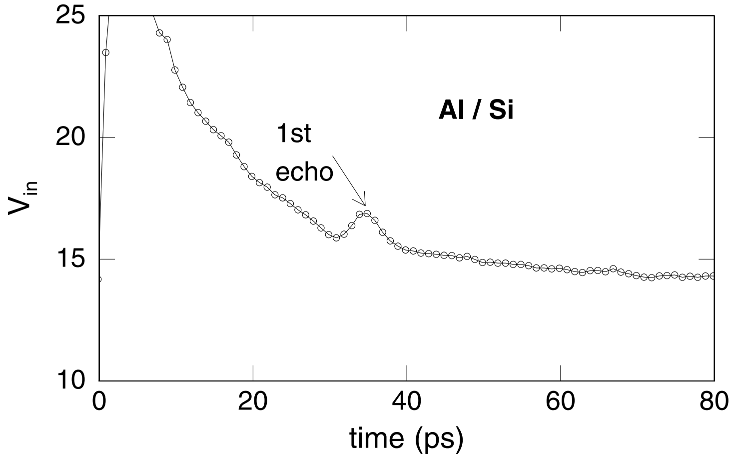

Figure 8. Picosecond acoustics measurements for an Al film deposited on Si (100) substrate. Arrival time of echo from the Al / Si interface is t_1 = 34.8 ps. Al layer thickness estimated from this measurement is $h_{Al} = v_{Al} t_1 / 2$ = 111.7 nm. Measurement was performed at f = 9.8 MHz.

In Figure 8, acoustic impedance of Si substrate [56] (ρ = 2.3 g cm^{-3}, v_{Si} = 8.4 nm ps^{-1}) is larger then that of the Al layer. The strain wave undergoes a null phase change at Al / Si interface so the sign of the echo peak is positive.

In some samples the shape of the first echo peak from the Al / sample interface consists of a combination of two peaks. I attribute this behavior to a thin soft layer of hydrocarbons or amorphous oxide created on the sample during subsequent handling in air before the Al deposition. I assume the acoustic impedance of the soft layer is less then that of the Al and sample layers; e.g., average values [55] for mass density and speed of sound of a hydrocarbon layer are $\rho = 1$ g cm^{-3} and $v = 2$ nm ps^{-1}.

Figure 9 illustrates the shape and sign of the first and second acoustic peaks resulting from reflections at Al / soft layer and soft layer / sample interfaces. The acoustic impedance of the soft layer is less then that of the Al and sample layers and the resulting reflections combine to form the peaks as shown in Figure 9c. An example of this behavior is shown in Figure 10, Figure 12 and Figure 15.

I measured the longitudinal cross-plane speed of sound for the sample layers in this study using the thickness of the layer (determined by XRR) and the time interval that separates acoustic echoes from the Al / sample interface and sample / substrate interface. Examples of the measurements for various samples used in my experiments are shown in Figure 10 to Figure 18. All measurements were performed with modulation frequency of the pump beam f = 9.8 MHz.

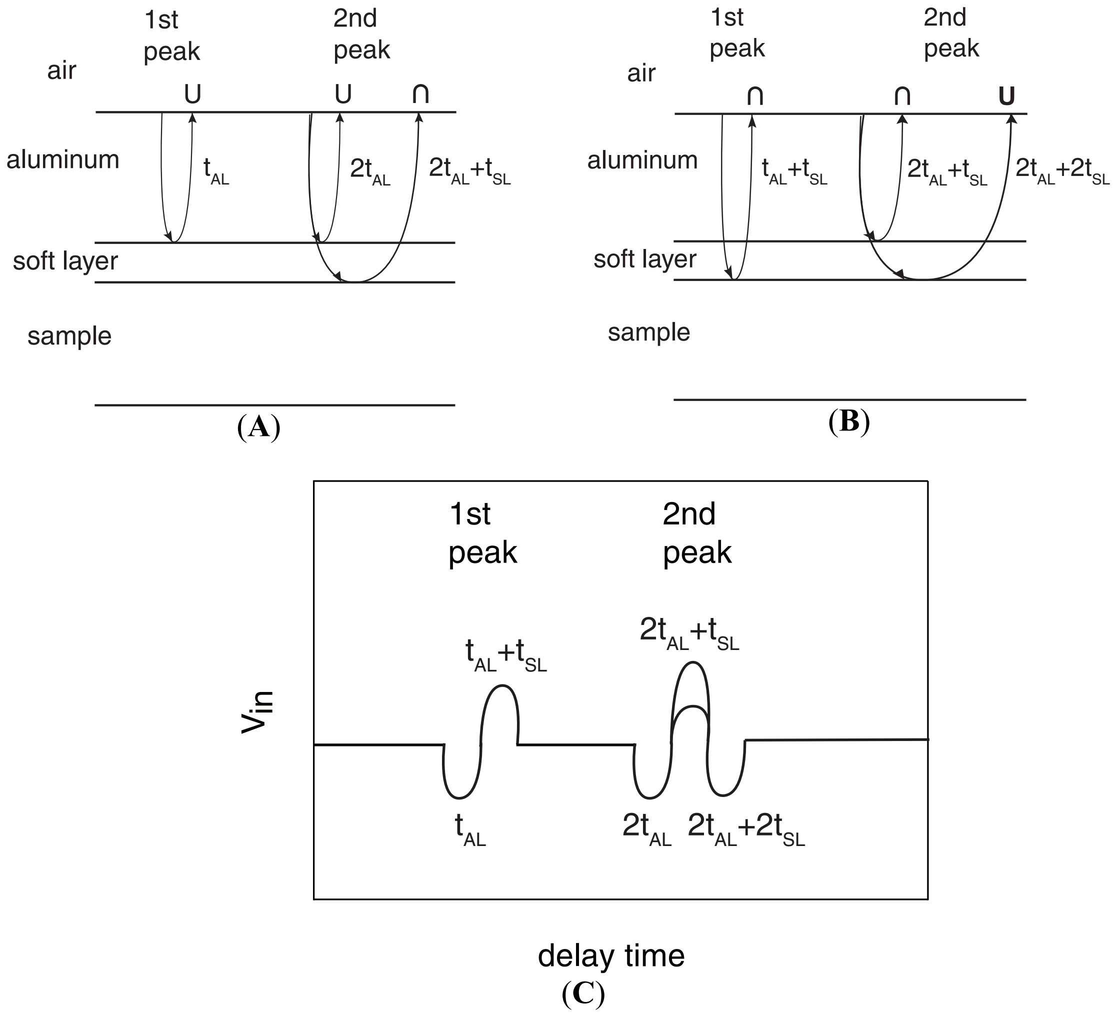

Figure 9. Illustrative sketch of acoustic reflections from Al / soft layer and soft layer / sample interfaces and their contributions to subsequent formation of the first and second Al acoustic peaks. The initial strain wave has two components: (A) one is reflected at the Al / soft layer and then undergoes secondary reflections at Al / soft layer and soft layer / sample interfaces; (B) the other is transmitted into the soft layer, is reflected off the soft layer / sample interface and then undergoes secondary reflections at Al / soft layer and soft layer / sample interfaces. The symbols "∪" and "∩" indicate the shape of the acoustic peak as a reflection reaches the surface of Al layer. Round times for crossing the thickness of Al layer (t_{AL}) and soft layer (t_{SL}) are used to calculate the arrival time of the reflections at the surface of Al layer. In Figure (C) is illustrated (not to scale) the predicted final shape and sign of the first and second acoustic peaks for the Al layer.

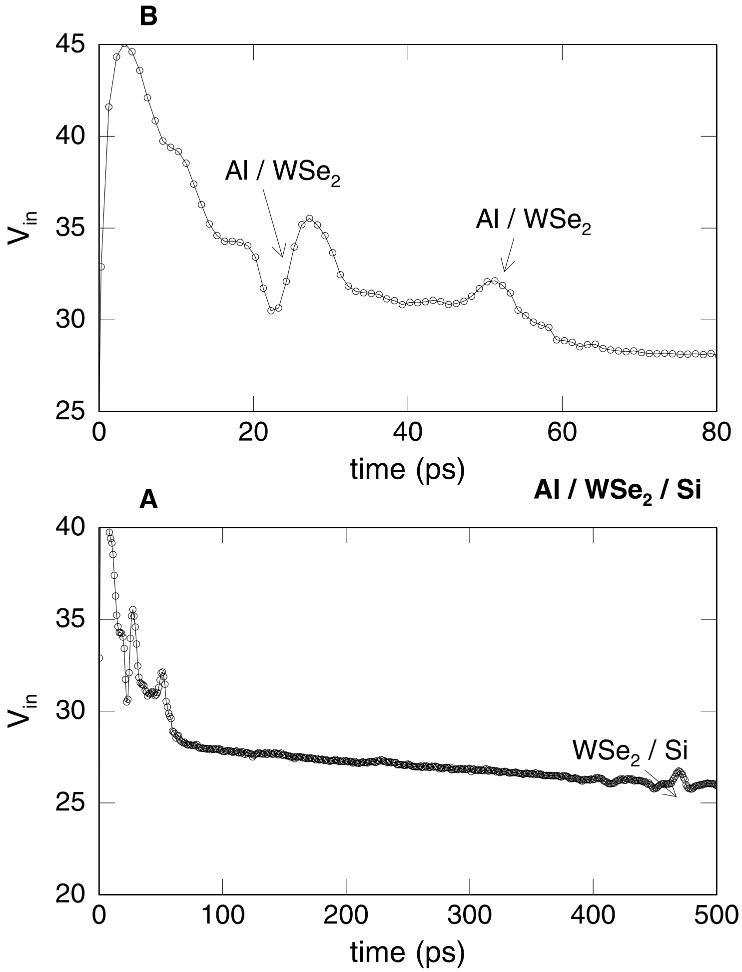

Figure 10. Picosecond acoustics measurements for h = 360 nm thick WSe_2 film deposited on Si (100) substrate and annealed to 625 ºC for 1 hour. The echoes from Al / WSe_2 interface are located at t_1 = 24.8 ps and t_2 = 51.3 ps (A). Arrival time for acoustic signal from WSe_2 / Si interface is t_3 = 469.2 ps (B). Cross-plane longitudinal speed of sound in the WSe_2 film is $v = 2\ h / (t_3 - t_1) = 1.6\ \text{nm ps}^{-1}$. Mass density of WSe_2 film from RBS measurements of areal density is $\rho = 9.35\ \text{g cm}^{-3}$. Top plot shows a detail of delay time range relevant for echoes from Al / WSe_2 interface. Average round time for the sound wave from the Al/WSe_2 interface to reach the surface of the Al layer is $t = (t_1 + t_2/2)/2$ = 25.2 ps. Thickness of Al layer is $h_{Al} = v_{Al}\ t / 2$ = 81 nm.

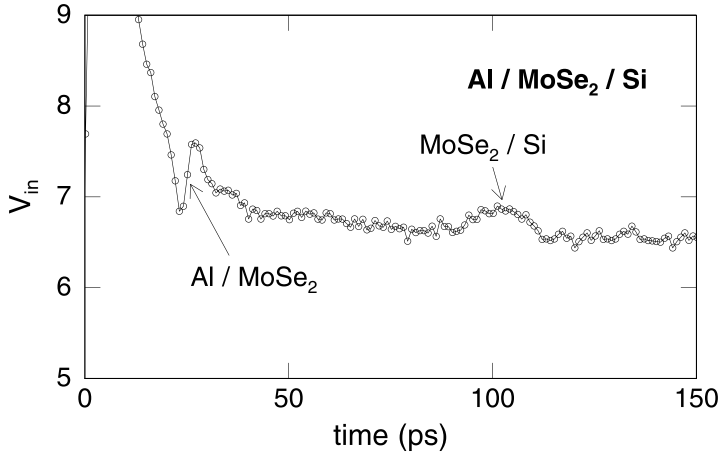

Figure 11. Picosecond acoustics measurements for h = 76 nm thick $MoSe_2$ film deposited on Si (100) substrate and annealed to 625 ºC for 1 hour. Arrival time of echoes from the Al / $MoSe_2$ and, respectively $MoSe_2$ / Si interfaces are t_1 = 25.2 ps and, respectively t_2 = 103.2 ps. Thickness of Al layer is $h_{Al} = v_{Al}\ t_1 / 2$ = 81 nm. Cross-plane longitudinal speed of sound in the $MoSe_2$ film is $v = 2\ h / t$ = 1.9 nm ps^{-1}. Mass density of $MoSe_2$ film from RBS measurements of areal density is ρ = 6.84 g cm^{-3}.

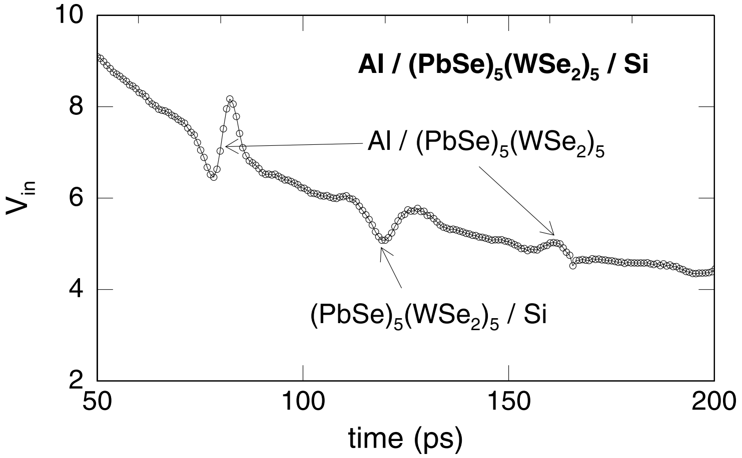

Figure 12. Picosecond acoustics measurements for h_{misfit_layer} = 59 nm thick misfit layered $(PbSe)_5(WSe_2)_5$ film deposited on Si (100) substrate and annealed to 400 ºC for 1 hour. Arrival time of echoes from the Al / $(PbSe)_5(WSe_2)_5$ interface are t_1 = 80 ps and t_2 = 161 ps. Average round time for the reflection from the Al / $(PbSe)_5(WSe_2)_5$ interface to reach the surface of the Al layer is $t = (t_1 + t_2/2)/2$ = 80.3 ps. Thickness of Al layer is $h_{Al} = v_{Al}\ t / 2$ = 257.6 nm. The echo from $(PbSe)_5(WSe_2)_5$ / Si interface is located at t_3 = 119.2 ps. Cross-plane longitudinal speed of sound in the $(PbSe)_5(WSe_2)_5$ film is $v_{misfit\_layer} = 2\ h_{misfit\_layer} / (t_3 - t_1)$ = 3 nm ps^{-1}. Mass density of $(PbSe)_5(WSe_2)_5$ film from RBS measurements of areal density is ρ = 7.25 g cm^{-3}.

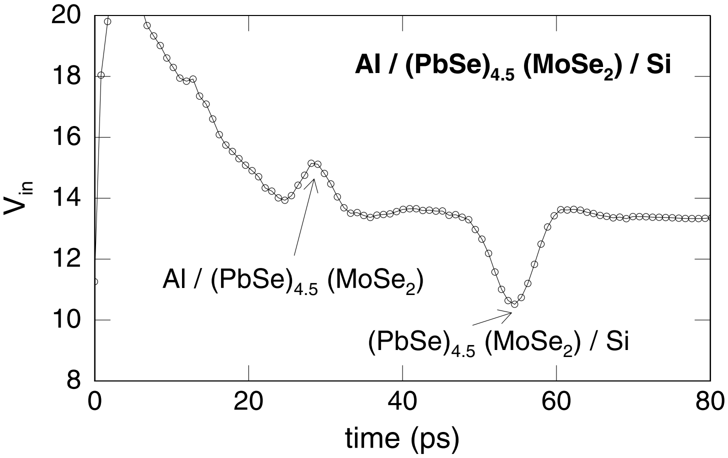

Figure 13. Picosecond acoustics measurements for $h_{misfit\_layer} = 44$ nm thick misfit layered $(PbSe)_{4.5}(MoSe_2)$ film deposited on Si (100) substrate and annealed to 400 ºC for 1 hour. The echoes from Al / $(PbSe)_{4.5}(MoSe_2)$ and $(PbSe)_{4.5}(MoSe_2)$ / Si interfaces arrive at surface of the Al layer at $t_1 = 28$ ps and, respectively $t_2 = 55$ ps. Thickness of Al layer is $h_{Al} = v_{Al}\, t_1 / 2 = 90$ nm. Cross-plane longitudinal speed of sound in the $(PbSe)_{4.5}(MoSe_2)$ film is $v_{misfit\_layer} = 2\, h_{misfit\_layer} / (t_2 - t_1) = 3.3$ nm ps^{-1}. Mass density of $(PbSe)_{4.5}(MoSe_2)$ film from RBS measurements of areal density is $\rho = 8.00$ g cm^{-3}.

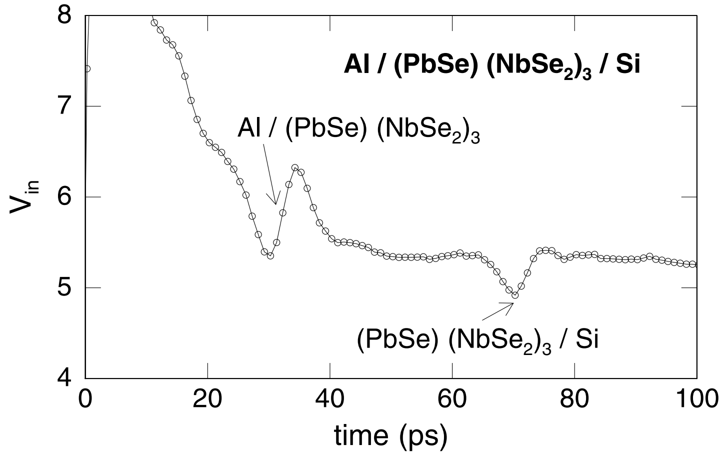

Figure 14. Picosecond acoustics measurements for h = 54 nm thick misfit layered $(PbSe)(NbSe_2)_3$ film deposited on Si (100) substrate and annealed to 400 ºC for 1 hour. Arrival time of echoes from the Al / $(PbSe)(NbSe_2)_3$ and $(PbSe)(NbSe_2)_3$ / Si interfaces are $t_1 = 32$ ps and, respectively $t_2 = 70$ ps. Thickness of Al layer is $h_{Al} = v_{Al}\, t_1 / 2 = 103$ nm. Cross-plane longitudinal speed of sound in the $(PbSe)(NbSe_2)_3$ film is $v = 2\, h / (t_2 - t_1) = 2.8$ nm ps^{-1}. Mass density of $(PbSe)(NbSe_2)_3$ film from RBS measurements of areal density is $\rho = 7.21$ g cm^{-3}.

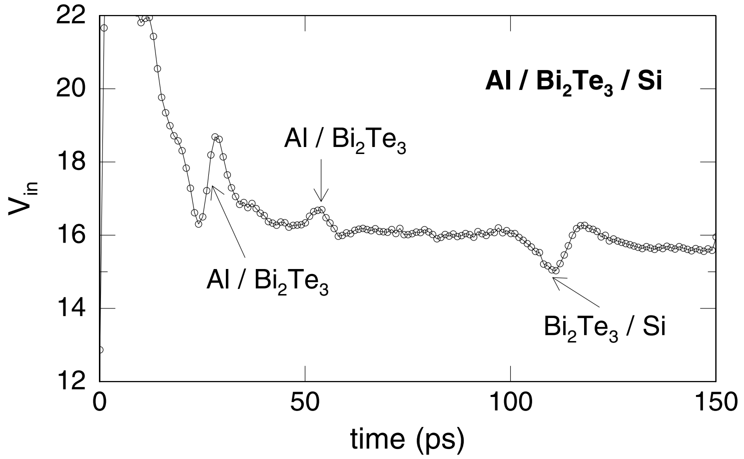

Figure 15. Picosecond acoustics measurements for h = 106 nm thick Bi_2Te_3 film deposited on Si (100) substrate and annealed to 400 ºC for 1 minute. The echoes from Al / Bi_2Te_3 interface are located at t_1 = 26.4 ps and t_2 = 53.1 ps. Arrival time for the echo from Bi_2Te_3 / Si interface is t_3 = 111 ps. Average round time for the reflection from the Al / Bi_2Te_3 interface to reach the surface of the Al layer is $t = (t_1 + t_2/2)/2 = 26.5$ ps. Thickness of Al layer is then $h_{Al} = v_{Al}\, t / 2 = 85$ nm. Cross-plane longitudinal speed of sound in the Bi_2Te_3 film is $v = 2\, h / (t_3 - t_1) = 2.5$ nm ps^{-1}. Mass density of Bi_2Te_3 film from RBS measurements of areal density is $\rho = 7.84$ g cm^{-3}.

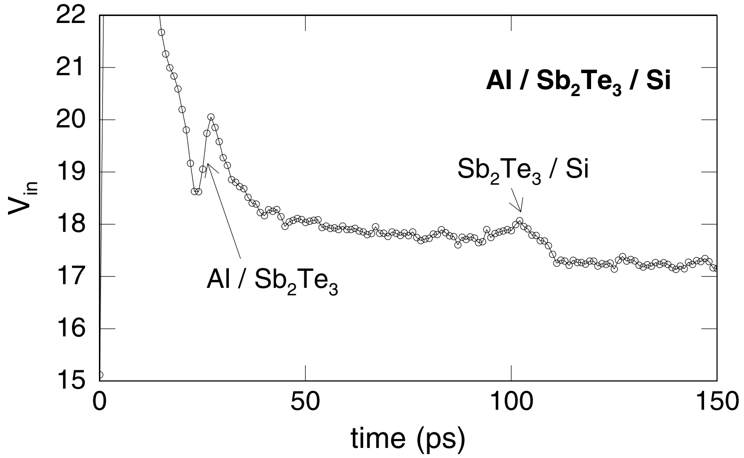

Figure 16. Picosecond acoustics measurements for h = 100 nm thick Sb_2Te_3 film deposited on Si (100) substrate and annealed to 400 ºC for 1 minute. The echoes from Al / Sb_2Te_3 and Bi_2Te_3 / Si interfaces are located at t_1 = 25.3 ps and, respectively t_2 = 103 ps. Thickness of Al layer is $h_{Al} = v_{Al}\, t_1 / 2 = 81$ nm. Cross-plane longitudinal speed of sound in the Sb_2Te_3 film is $v = 2\, h / (t_2 - t_1) = 2.6$ nm ps^{-1}. Mass density of Sb_2Te_3 film from RBS measurements of areal density is $\rho = 6.48$ g cm^{-3}.

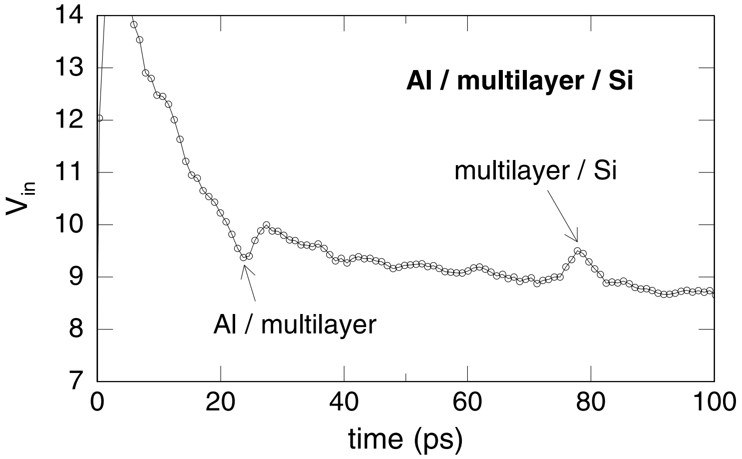

Figure 17. Picosecond acoustics measurements for h = 59 nm thick $(TiTe_2)_4(Bi_2Te_3)_3(TiTe_2)_4(Sb_2Te_3)_3$ multilayer film deposited on Si (100) substrate and annealed to 250 ºC for 5 minutes. Arrival time of echoes from the Al/multilayer interface and multilayer/Si interface are t_1 = 23.7 ps and, respectively t_2 = 77.8 ps. Al layer thickness estimated from this measurement is $h_{Al} = v_{Al}\ t_1 / 2$ = 76 nm. Cross-plane longitudinal speed of sound in the 3-component multilayer film is $v = 2\ h / (t_2 - t_1)$ = 2.2 nm ps^{-1}. Mass density of $(TiTe_2)_4(Bi_2Te_3)_3(TiTe_2)_4(Sb_2Te_3)_3$ multilayer film from RBS measurements of areal density is ρ = 7.01 g cm^{-3}.

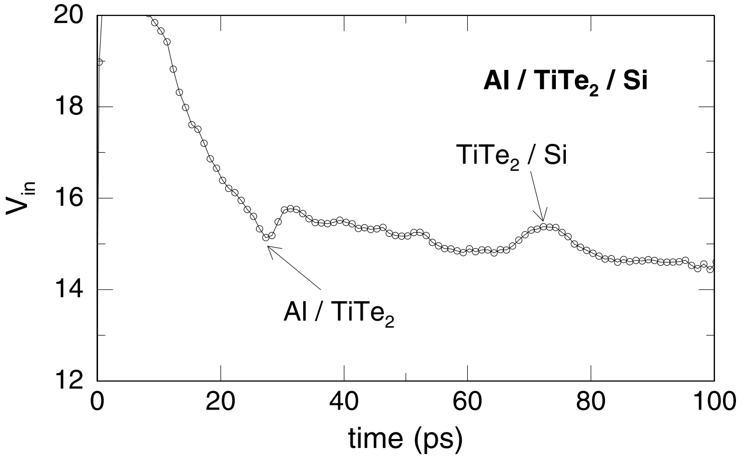

Figure 18. Picosecond acoustics measurements for h = 44 nm thick $TiTe_2$ film deposited on Si (100) substrate and annealed to 300 ºC for 5 minutes. Arrival time of echoes from the Al / $TiTe_2$ and $TiTe_2$ / Si interfaces are t_1 = 27.8 ps and, respectively t_2 = 73.3 ps. Al layer thickness estimated from this measurement is $h_{Al} = v_{Al}\ t_1 / 2$ = 89 nm. Cross-plane longitudinal speed of sound in the $TiTe_2$ film is $v = 2\ h / (t_2 - t_1)$ = 1.9 nm ps^{-1}. Mass density of $TiTe_2$ film from RBS measurements of areal density is ρ = 6.25 g cm^{-3}.

To estimate the accuracy of measuring speed of sound in a layer by picosecond acoustics, I add the uncertainties in measuring the thickness of the layer (~5%) and the time interval between successive echoes (~ 5%). Overall accuracy for measuring speed of sound is 10%.

Picosecond interferometry is based on inelastic light scattering from acoustic modes, i.e., Brillouin scattering. The frequency shift of the scattered light is known as the Brillouin frequency φ. In this method, a semitransparent ~ 10 nm thin film of Pd is deposited on the samples. The wavelength of the Ti : sapphire laser is adjusted to a center peak value where the sample is transparent. Thermal expansion of Pd film due to heating by the pump laser pulses generates a strain pulse. Interference of probe pulses reflected from the strain pulse and the Pd surface creates periodic oscillations of frequency φ in the in-phase signal V_{in}. The longitudinal speed of sound v is determined then by $v = \varphi \lambda / 2n$, where n is the index of refraction and λ the laser wavelength. The index of refraction is determined by variable angle spectroscopic ellipsometry (VASE). An example of picosecond interferometry measurement data is shown in Figure 19. Overall uncertainty in determining the speed of sound by picosecond interferometry is 5% and is dominated by the errors in measuring the index of refraction n.

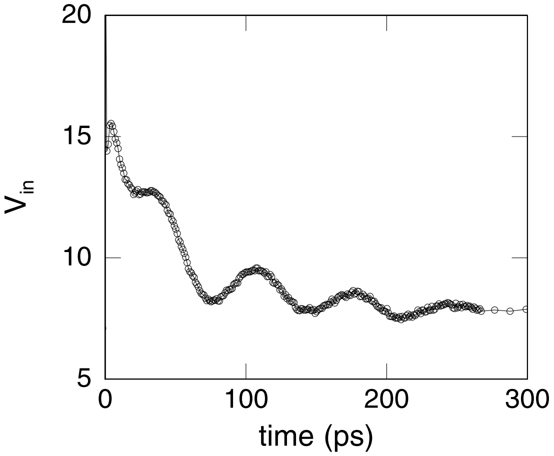

Figure 19. Example data for the oscillations in V_{in} as a function of delay time that are used to measure longitudinal speed of sound by picosecond interferometry in a 343 nm thick WSe_2 film. Laser wavelength is 800 nm, the period of oscillations is 60 psec and index of refraction measured by VASE is n = 4.13; speed of sound $v = 1.61$ nm ps^{-1}.

CHAPTER 3

THERMAL CONDUCTIVITY OF HOMOGENOUS, LAYERED DISORDERED CRYSTALLINE MATERIALS

Significant components of this chapter were published in “Ultralow thermal conductivity in disordered, layered WSe_2 crystals”, Science 315 (351) 2007. I collaborated with Professor David Johnson, Dr. Nguyen Ngoc and Mr. Colby Heideman at University of Oregon for sample deposition. Dr. Paul Zschack at the Advanced Photon Source at Argonne National Laboratory provided instrument time and assistance with synchrotron x-ray characterization of the deposited films. I deposited some of the samples used in this study and I performed laboratory x-ray diffraction, ion bombardment, RBS elemental analysis and the thermal and elastic properties measurements.

3.1 Introduction

The lowest thermal conductivity materials are typically found among electrically-insulating amorphous solids and glasses. In these materials, heat conduction is adequately predicted by a simple phenomenological model, the minimum thermal conductivity, where heat conduction is described by a random walk of vibrational energy on the time and length-scales of atomic vibrations and inter-atomic spacings [4]. More sophisticated theories of heat conduction in disordered materials support this description: a majority of the vibrational modes (termed “diffusons” by Allen and Feldman [57]) carry heat in this manner and only a small fraction of the vibrational modes propagate as waves, or are localized and therefore unable to contribute to heat conduction. Recent reports [58, 59] have shown that the minimum thermal conductivity can be circumvented in multilayer thin films of metals and oxides. When the spacing between the interfaces is only a few nm, the thermal resistance of the interfaces reduces the thermal conductivity far below the thermal conductivity of the homogeneous amorphous oxide.

In this section, I demonstrate a new route for achieving ultra-low thermal conductivity. The thermal conductivity of disordered thin films of the layered crystal WSe_2 can be as small as 0.05 W m^{-1} K^{-1}, a factor of 6 smaller than the predicted the minimum thermal conductivity and, to the best of my knowledge, the lowest thermal conductivity ever observed in a fully dense solid. Disruption of the layered structure and the crystallinity of the WSe_2 sheets by ion irradiation produce a dramatic increase in the thermal conductivity of the thin film. Thus, the lowest thermal conductivities are not found in the fully amorphous form of WSe_2; rather, ultra-low thermal conductivity is achieved by controlling both order and disorder in this anisotropic material.

3.2 Experimental Details

Thin films of tungsten selenide (WSe_2, nominal thickness 30, 50, 70, 360 and 480 nm), molybdenum selenide ($MoSe_2$, nominal thickness 70 and 260 nm) and niobium selenide ($NbSe_2$, nominal thickness 30, 60, and 120 nm) were synthesized by the modulated elemental reactants (MER) method. Sequential bilayers of M (M=W, Mo, Nb) and Se were deposited onto unheated Si (100) wafers. In each bilayer, the ratio of the layer thicknesses was adjusted such that, after annealing, we obtain the stoichiometry of the desired compound: 1.4Å of M (M=W, Mo or Nb) and 9Å of Se per bilayer. I purchased a single crystal of WSe_2 from Nanoscience Instruments to provide a baseline for comparisons. The Si wafers used for $MoSe_2$ deposition had a 50 nm thick thermally grown a-SiO_2 blanket layer.

The base pressure of the deposition chamber was 10^{-7} torr. Molybdenum, niobium and tungsten were deposited using electron-beam sources (99.95% purity); selenium (99.995% purity) was evaporated from effusion cells.

After deposition, the samples were annealed in a N_2 atmosphere to form the desired layered structures. WSe_2 films of nominal thickness of 30, 50, and 360 nm were annealed for 1 h at 625 °C. To investigate how the microstructure and thermal conductivity evolved with annealing, films of nominal thickness of 70 nm were annealed for 1 hour at 200, 350, 500 and 650 °C; and films of nominal thickness 480 nm were annealed for 4 hours at 300, 400, 500 and 600 °C; $MoSe_2$ films were annealed at for 1 hour at 250, 450 and 625 °C; $NbSe_2$ films were annealed at for 1 hour at 100, 200, 300 and 400 °C.

The crystalline quality and crystallographic orientation were evaluated by x-ray diffraction (XRD) using a Philips X'pert diffractometer with Cu $K\alpha 1$ radiation; instrumental broadening determined from the FWHM of the (004) peak of a Si standard is 0.18 degrees.

Synchrotron x-ray diffraction provided an in-depth look at the microstructure of the samples. The scans were taken at the high-resolution 33ID beam line of the Advanced Phonon Source (APS) at Argonne National Laboratory. The scans were collected at beam energies of 13.4 keV and 18.5 keV. In-plane diffraction is a technique that is sensitive to the in-plane (*a-b* lattice plane) structure of the films. The data was collected by setting the sample on a goniometer (Huber or Newport Kappa Diffractometer) at a small incident angle (0.20 degrees) relative to the x-ray source and scanning the detector in the *a-b* plane of the film. Scans of reciprocal space were obtained using a MAR345 (Rayonix/ Marresearch) scanning image plate detector at a grazing incidence angle of 1.0. The raw image plate data consists of a 2300 x 2300 matrix that consists of pixels of intensity (z coordinate) with x and y coordinates. To obtain useful information, the data must be calibrated to account for the detector to sample distance, x-ray wavelength, tilt of the detector and the distortion of the Ewald sphere due to using a flat image plate. The acquired data was processed and converted to reciprocal space plots using Fit2D software [60].

The stoichiometry and oxygen contamination of the films were determined by EPMA. Oxygen content was on average 3 at.% in all the samples. Thickness of the films was determined from low angle (< 10 degrees 2θ) XRR scans by analyzing the Kiessig fringes.

I measured thermal conductivity using time-domain thermoreflectance; a thin film of Al, 60-85 nm thick was deposited on the samples by dc magnetron sputtering. Because of the very low thermal diffusivity of samples, I optimized the sensitivity of my measurements (see Figure 6) by using different pump beam modulation frequencies: I used a low frequency (580 kHz) for the 30, 50, and 70 nm WSe_2 films, the 70 nm $MoSe_2$ films and the 30 and 60 nm $NbSe_2$ films. I used a high frequency (9.8 MHz) for the 360 and 480 nm WSe_2 films and the single crystal WSe_2 sample, the 260 nm $MoSe_2$ films and the 120 nm $NbSe_2$ films. The pump and probe beam optical beams were focused on the surface of the samples using a microscope objective lens of 40 mm focal length, producing a $1/e^2$ radius of the focused spot of 14 microns. The laser power incident at the surface of the sample is typically ~ 5 mW for both the pump and probe. The steady-state temperature rise at the surface of the thin film samples is typically ~ 5 K with the highest steady-state temperature rise encountered in my experiments being 10 K for a 343 nm WSe_2 film at 88 K. For the single-crystal WSe_2 sample, the highest steady state temperature rise encountered in my experiments is 20 K at a measurement temperature of 300 K. The steady-state heating of the samples is taken into account in the data analysis.

The thermal conductivity is determined by comparing the time dependence of the ratio of the in-phase V_{in} and the out-of-phase V_{out} signals from the rf lock-in amplifier to calculations using a thermal model. The thermal model has several parameters (pump modulation frequency, laser spot size, and the thickness, thermal conductivity and heat capacity of each layer) but the thermal conductivity of the sample film or bulk crystal is the only important unknown. The aluminum film thickness was derived using the picosecond acoustics method. Aluminum thermal conductivity is calculated using the Wiedemann-Franz law from 4-point probe measurements of the electrical resistivity at 300 K; lower temperature values were estimated from the values at 300 K assuming a constant residual resistivity [30]. The heat capacity of the Al layer [31], and heat capacity [32] and thermal conductivity [33] of the Si substrate are taken from literature values. I used reference literature values for temperature dependence of heat capacity for WSe_2 [38], $MoSe_2$ [39] and $NbSe_2$ [40]. The thermal conductance of the Al/sample interface is also adjusted in the model to fit the data but because of the low thermal conductivities of the thin films, this interface conductance has very little influence on the measurement of the thermal conductivity. Overall uncertainties range between 10% at 300 K and 25% at 80 K.

I measured the cross-plane longitudinal speed of sound v_L in the films using picosecond acoustics; v_L is determined from the sample thickness measured by x-ray reflectivity and the difference in the arrival times of acoustic echoes reflected from the Al/sample and sample/substrate interfaces.

To study the effect of order-disorder balance I bombarded a sample of 24 nm WSe_2 film with 1 MeV Kr^+ ion beam. The fluences used were in the range of $1x10^{13}$ to $3x10^{15}$ cm^{-2}. A low beam current (30 nA) was used to minimize the amount of self-annealing in the samples. Simulations using the Ion Stopping and Range in Targets module in SRIM 2008 software package [61] predict that 1 MeV Kr^+ ions pass thru the 24 nm thick $WeSe_2$ films and penetrate deep into the Si substrate to a range of ~ 600 nm. To convert the Kr^+ fluence to units of displacement per atom (DPA) for each layer of the target, I calculated the depth profile of collision events using SRIM software package with displacement energies 25 eV for WSe_2 and 15 eV for Si. The profile is then converted to DPA for each respective dose/layer type (see Figure 20 and Figure 21). The effect of the WSe_2 layer on the DPA depth distribution is negligible because its thickness is much smaller than the projected range of Kr^+ ions in the entire target.

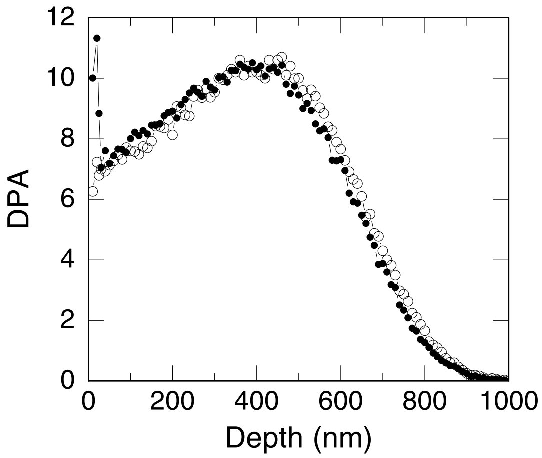

Figure 20. Calculated depth profile of DPA for 1 MeV Kr^+ ions in Si for ions dose of $3x10^{15}$ ions/cm^2. Open circles indicate the simulated profile in a Si substrate only, closed circles indicate the profile for a target composed of 24 nm WSe_2 on top of a Si substrate. The DPA plot of the 24 nm of WSe_2 is expanded in Figure 21.

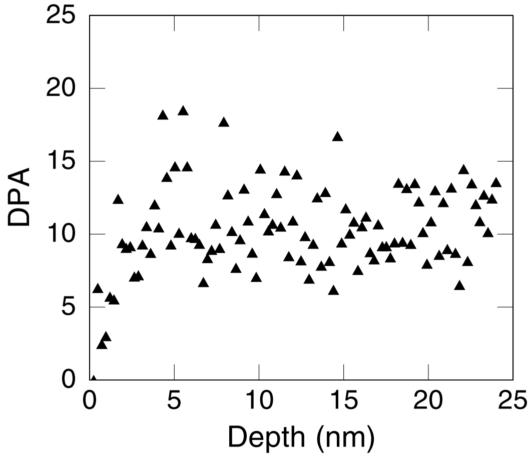

Figure 21. Calculated depth profile of DPA for 1 MeV Kr^+ ions in 24 nm WSe_2 film for ion dose of $3x10^{15}$ ions/cm^2.

I irradiated bare silicon substrates with the same range of ion fluences and measured their thermal conductivity using the TDTR method. For TDTR data analysis the irradiated bare substrates were modeled as a 600 nm top layer of uniformly [62] amorphized Si (the length of ion penetration depth) and a bottom layer of crystalline Si. The measured thermal conductivity of ion-irradiated Si (Figure 22 and Figure 23) was then used in the TDTR analysis of the WSe_2 films.

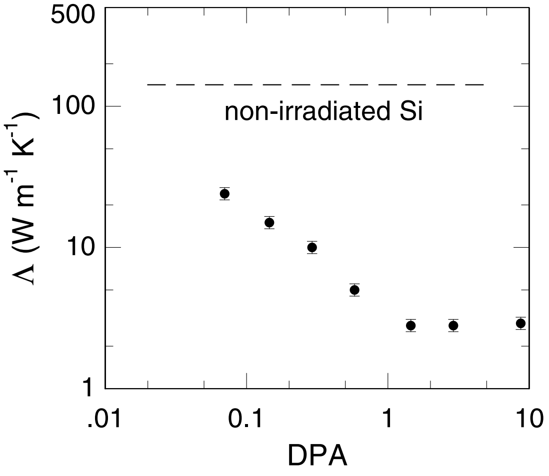

Figure 22. Thermal conductivity Λ versus irradiation dose (DPA units) for bare Si substrate. Each DPA value is obtained from the calculated DPA depth profile for each respective irradiation dose by averaging over a distance of 600 nm.

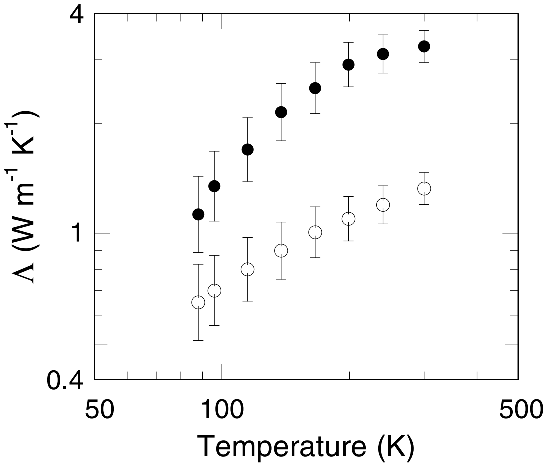

Figure 23. Thermal conductivity Λ (closed circles) versus temperature for bare Si substrate irradiated with 1 MeV Kr$^+$ ions to a dose of 3x10^{15} cm^{-2} (DPA = 8.72). Also included is the temperature dependence of thermal conductivity (open circles) for a 1 μm thick a-SiO$_2$ film from Figure 5.

3.3 Results and Discussion

Structure analysis of the samples by x-ray diffraction (XRD) using a laboratory x-ray source shows that the films have a layered structure with as-deposited samples containing weak and broad (0 0 L) diffraction maxima; the intensity and sharpness of these diffraction peaks grow with annealing temperature (see Figure 24, Figure 25 and Figure 26).

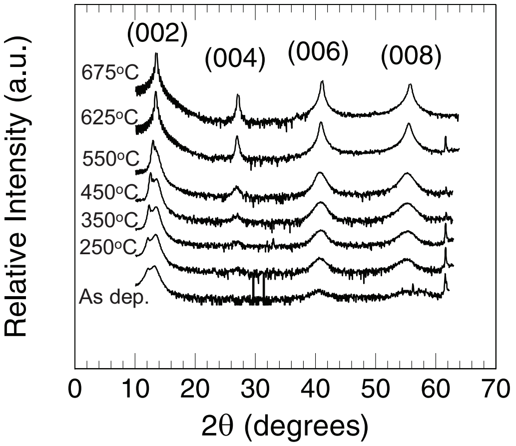

Figure 24. X-ray diffraction data as a function of annealing temperature for a 50 nm WSe_2 thick film, annealed for 1 h in dry nitrogen atmosphere at the temperatures indicated in the plot. (0 0 L) peaks are indexed in the figure.

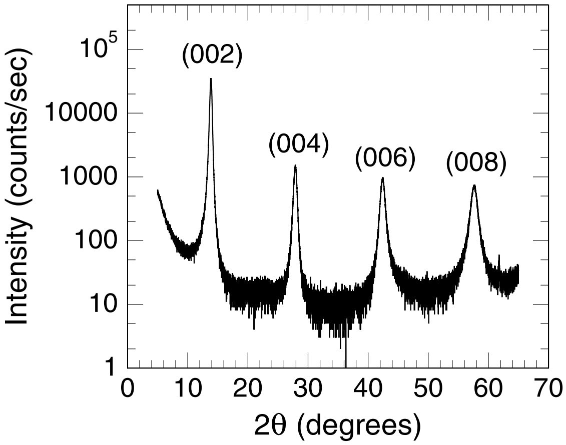

Figure 25. X-ray diffraction data for a 60 nm $NbSe_2$ thick film, annealed for 1 h in dry nitrogen atmosphere at 400 ºC. (0 0 L) peaks are indexed in the figure.

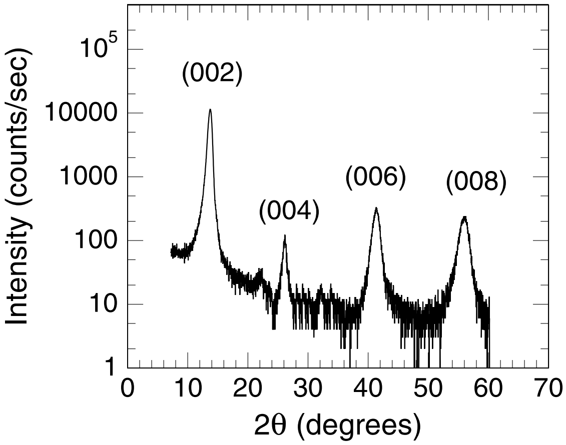

Figure 26. X-ray diffraction data for a 70 nm $MoSe_2$ thick film, annealed for 1 h in dry nitrogen atmosphere at 625 ºC. (0 0 L) peaks are indexed in the figure.

I analyzed the stoichiometry and areal density of the sample films using RBS (see Figure 27). The conversion factors used to convert channel to energy in Figure 27 are: WSe_2 – calibration offset 138 keV and energy per channel 1.82 eV/ch; $NbSe_2$ – calibration offset 134 keV and energy per channel 1.82 eV/ch; $NbSe_2$ – calibration offset 136.5 keV and energy per channel 1.85 eV/ch. The quadratic term was null for all measurements. Overall accuracy for estimating the stoichiometry of the sample layers is 1.4% (see Section 2.2).

The ratio of metal (W, Mo or Nb) to chalcogenide (Se) in the samples increases with annealing temperature from $x = 0.39 \pm 0.01$ in the as-deposited samples to $x = 0.49 \pm 0.01$ in the samples annealed to the highest temperatures (about 600 ºC for WSe_2 and $MoSe_2$ and 400 ºC for $NbSe_2$). Mass density of the thin film samples was determined from RBS measurements of total areal density of atoms (see section 2.2) and number density of atoms N for each material. Mass density increases with annealing temperature from 98.5 to 99.8% of theoretical density: $\rho = 9.39$ g cm^{-3} for WSe_2, $\rho = 6.97$ g cm^{-3} for $MoSe_2$, and $\rho = 6.47$ g cm^{-3} for $NbSe_2$.

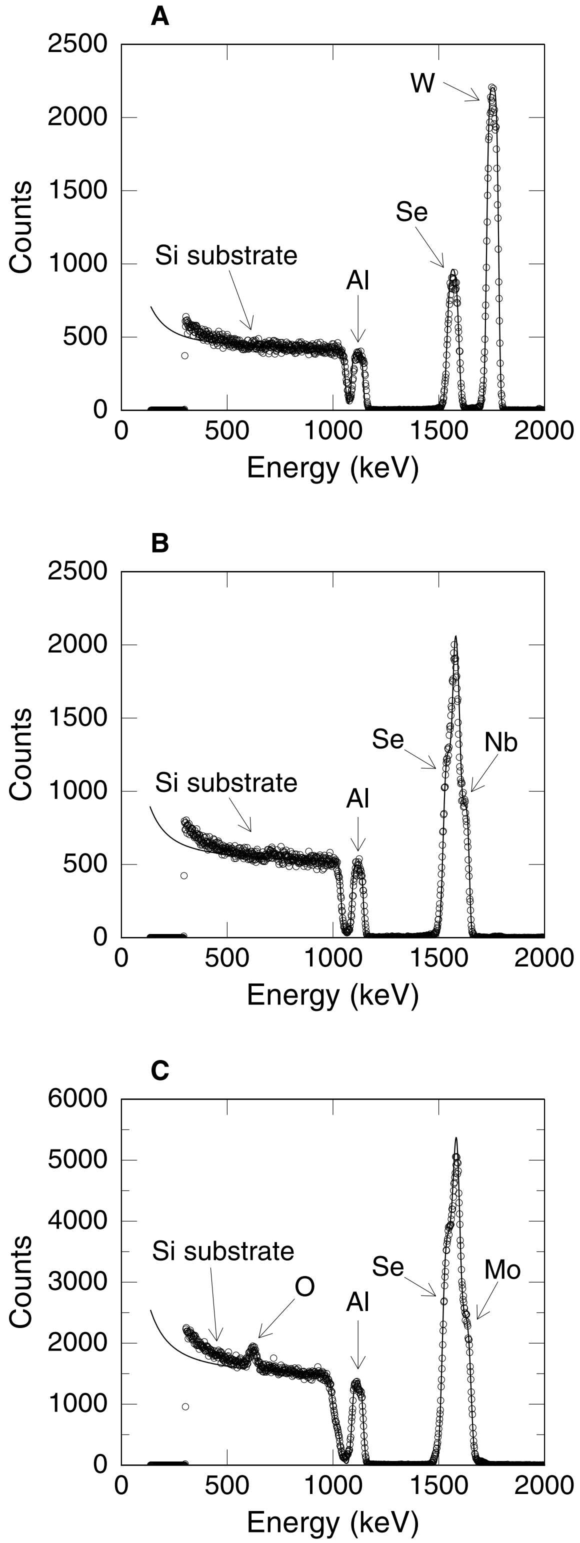

Figure 27. RBS spectra (open circles) and the SIMNRA fit (uninterrupted line) for (A) 50 nm thick WSe_2 sample; (B) 60 nm thick $NbSe_2$ film; (C) 70 nm thick $MoSe_2$ film; oxygen peak in Figure C belongs to 50 nm a-SiO_2 thermally grown on the Si substrate.

The XRD and RBS observations indicate that the desired chemical compounds are fully formed after deposition and undergo further densification and crystallization with annealing temperature.

I used synchrotron x-ray diffraction to characterize the microstructure of a typical WSe_2 film. These highly textured films have completely random crystalline orientation in the *a-b* plane. I examined the crystalline structure of the film by scanning the diffraction intensity through reciprocal space where the (1 0 3) reflection intersects the Ewald sphere. The relatively narrow linewidth in the direction parallel to the surface, [H 0 3], gives a lateral coherence length of 6 nm (Figure 28C). Scans through the intersection of (1 0 L) reflections with the Ewald sphere probe the coherence of the crystal structure along the direction normal to the WSe_2 sheets. The large linewidths (Figure 28B) indicate that crystallographic ordering in the stacking of the WSe_2 sheets is limited to <2 nm.

Similar scans on a typical $NbSe_2$ thin film (Figure 29) yields in-plane coherence length of 9 nm and out-of-plane coherence length of 3 nm. Scans of $MoSe_2$ (Figure 30) thin film samples result in in-plane coherence length of 5 nm and out-of-plane coherence length of 2 nm.

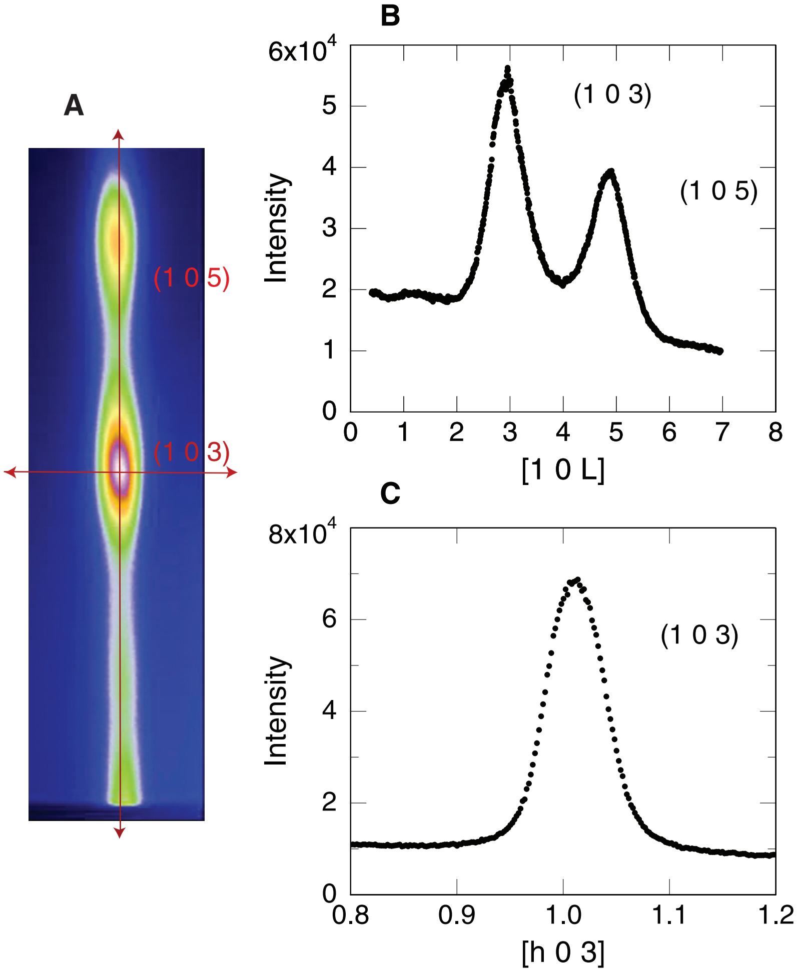

Figure 28. X-ray diffraction data for a 32.5 nm thick WSe_2 film collected at the 33BM beam-line of the Advanced Photon Source using 18.5 keV photons. After deposition, the WSe_2 film was annealed for 1 hour at 650°C in a N_2 atmosphere. (A) False-color depiction of the x-ray diffraction intensities collected by the area detector in the vicinity of the (1 0 3) and (1 0 5) reflections. The vertical direction is normal to the sample surface and the horizontal direction is in the plane of the sample. (B) Scan of the x-ray diffraction intensities along the surface normal. The scan direction is shown as the vertical red line in A). (C) Scan of the x-ray diffraction in the in-plane direction. The scan direction is shown as the horizontal red line in (A).

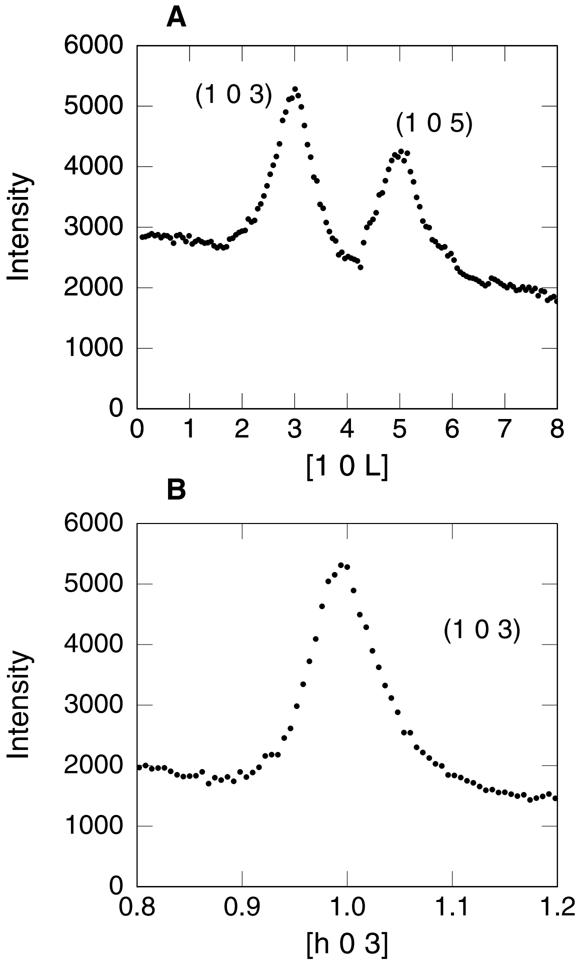

Figure 29. X-ray diffraction data for a 60 nm thick $NbSe_2$ film collected at the 33ID beam-line of the Advanced Photon Source using 13.4 keV photons. After deposition, the $NbSe_2$ film was annealed for 1 hour at 400°C in a N_2 atmosphere. (A) Scan of the x-ray diffraction intensities along the surface normal. (B) Scan of the x-ray diffraction in the in-plane direction.

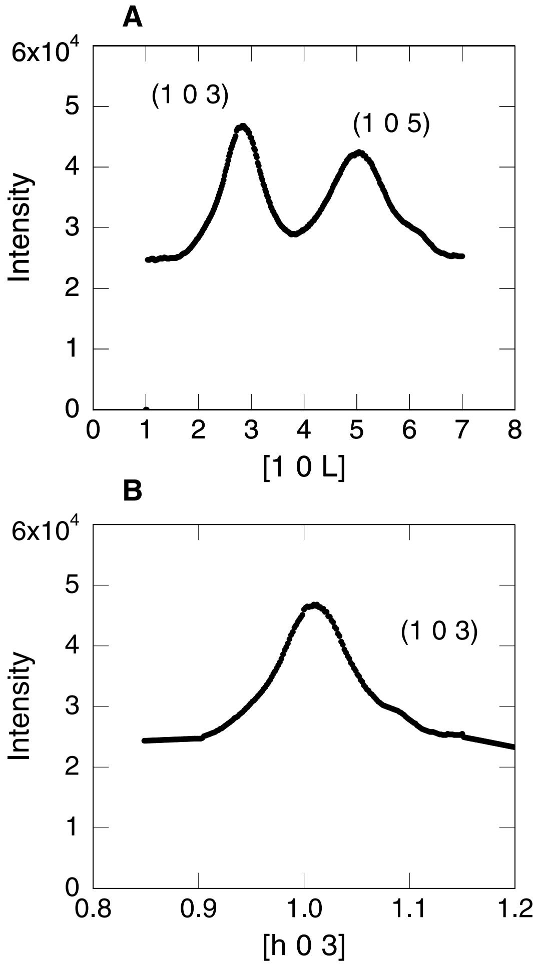

Figure 30. X-ray diffraction data for a 70 nm thick $MoSe_2$ film collected at the 33ID beam-line of the Advanced Photon Source using 13.4 keV photons. After deposition, the $MoSe_2$ film was annealed for 1 hour at 625°C in a N_2 atmosphere. (A) Scan of the x-ray diffraction intensities along the surface normal. (B) Scan of the x-ray diffraction in the in-plane direction.

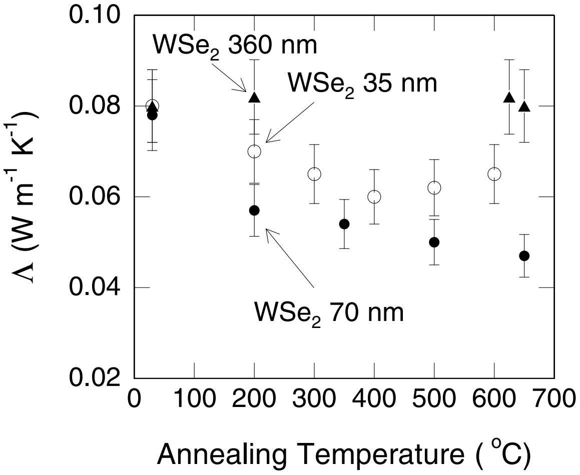

Figure 31. Thermal conductivity Λ vs. annealing temperature for WSe_2 films with nominal thicknesses 70 nm (full circles), 360 nm (closed triangles) and 35 nm (open circles). Annealing was done in N_2 atmosphere for one hour at the temperature indicated on the x-axis.

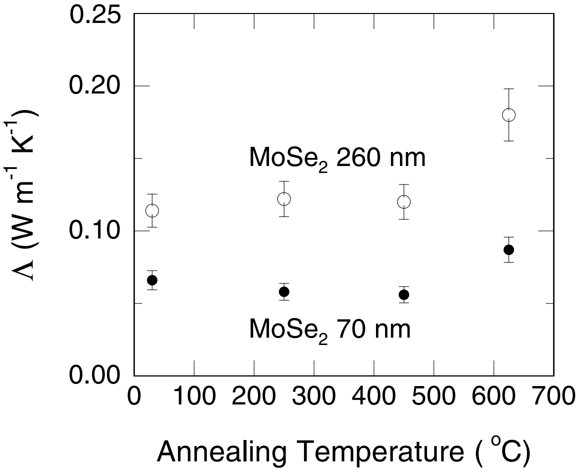

Figure 32. Thermal conductivity Λ vs. annealing temperature for $MoSe_2$ films with nominal thicknesses 70 nm (full circles) and 260 nm (open circles). Annealing was done in N_2 atmosphere for one hour at the temperature indicated on the x-axis.

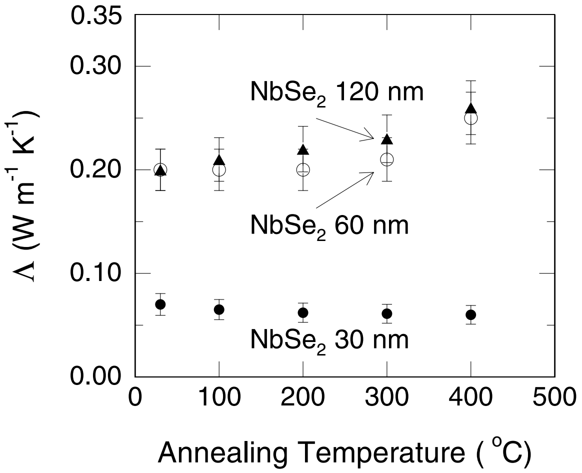

Figure 33. Thermal conductivity Λ vs. annealing temperature for $NbSe_2$ films with nominal thicknesses 30 nm (full circles), 60 nm (open circles) and 120 nm (closed triangles). Annealing was done in N_2 atmosphere for one hour at the temperature indicated on the x-axis.

Data for thermal conductivity as a function of annealing temperature demonstrate that microstructure evolution in 70 nm thick WSe_2 samples during thermal annealing causes the thermal conductivity to decrease (Figure 31). This behavior is surprising: since annealing materials at elevated temperature reduces the densities of metastable crystalline defects and thermal conductivity tends to increase as defects are eliminated, it is typically expected that annealing a material will increase the thermal conductivity. A similar behavior is observed in 70 nm thick $MoSe_2$ samples (see Figure 32) and 30 nm thick $NbSe_2$ samples (see Figure 33).

In Figure 34, I compare the thermal conductivity of annealed WSe_2 films to the conductivity of a single crystal of WSe_2 and the predicted minimum thermal conductivity. The thermal conductivity of single crystal WSe_2 is approximately proportional to 1/T, as expected for a dielectric or semiconductor where heat transport is dominated by phonons with mean-free-paths limited by anharmonicity. Calculations of the minimum thermal conductivity require knowledge of the number density of atoms and the speeds of sound [4]. Number density of atoms calculated from lattice parameters is $N = 4.96\text{x}10^{22}$ atoms cm^{-3}. I measured the longitudinal speed of sound in the cross-plane direction of nominal 360 nm thick films, $v_L = 1.6$ nm ps^{-1}, using picosecond acoustics; this measurement is in good agreement with an independent measurement of the same film using picosecond interferometry, $v_L = 1.7$ nm ps^{-1}, using an index of refraction at the laser wavelength of 800 nm of $n = 4.13$. Using v_L=1.65 nm ps^{-1} and a mass density of 9.4 g cm^{-3}, gives the elastic constant C_{33}=25.6 GPa, comparable to C_{33} literature values for $NbSe_2$ and $TaSe_2$ [63]. The transverse speed of sound v_T is not accessible to the standard methods of picosecond acoustics; instead, I estimated v_T=1.15 nm ps^{-1} from the measurement of v_L and the literature ratio C_{44}/C_{33} for $NbSe_2$ and $TaSe_2$.

The lowest thermal conductivity Λ measured at 300 K is $\Lambda = 0.048$ W m^{-1} K^{-1} for a 62 nm thick WSe_2 film, 30 times smaller than the cross-plane thermal conductivity of single-crystal sample of WSe_2 (Figure 34) and a factor of 6 smaller than the predicted minimum thermal conductivity. This degree of deviation from the predicted minimum thermal conductivity in a homogeneous material is unprecedented [64]. Interestingly, the conductivity of the 62 nm thick film is smaller than the conductivity of a thinner film (24 nm) or a thicker film (343 nm). The reasons for these differences are not understood at this time but it might be due to variations in the degree of crystallographic ordering along the thickness of the films.

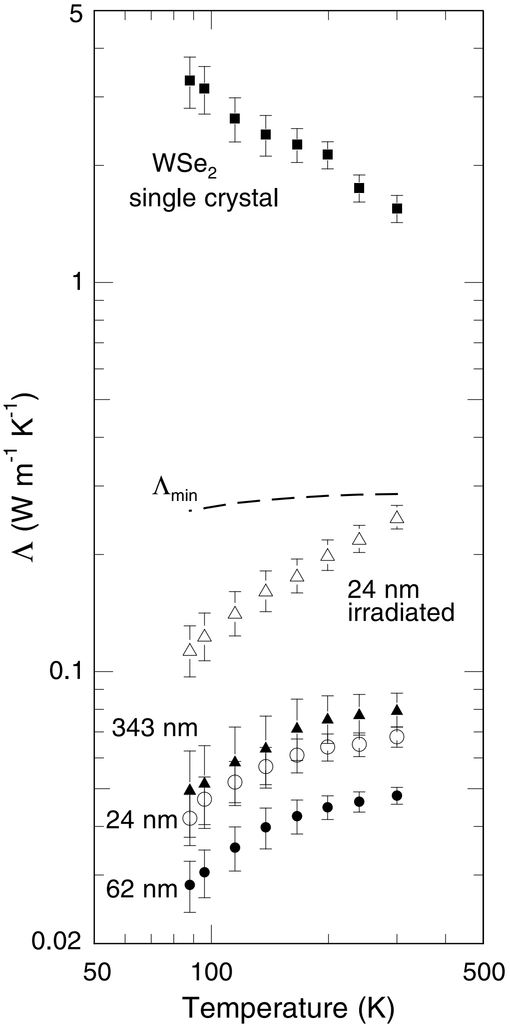

Figure 34. Summary of measured thermal conductivities of WSe$_2$ films as a function of the measurement temperature. The samples were annealed at 625 ºC for 1 hour prior to measurements. Each curve is labeled by the film thickness. Data for a bulk single crystal are included for comparison. The ion-irradiated sample was subjected to a 1 MeV Kr$^+$ ion dose of 3x10^{15} cm^{-2} (~ 10.5 DPA). The interrupted line marked Λ_{min} is the calculated minimum thermal conductivity for Wse$_2$ films in the cross-plane direction.

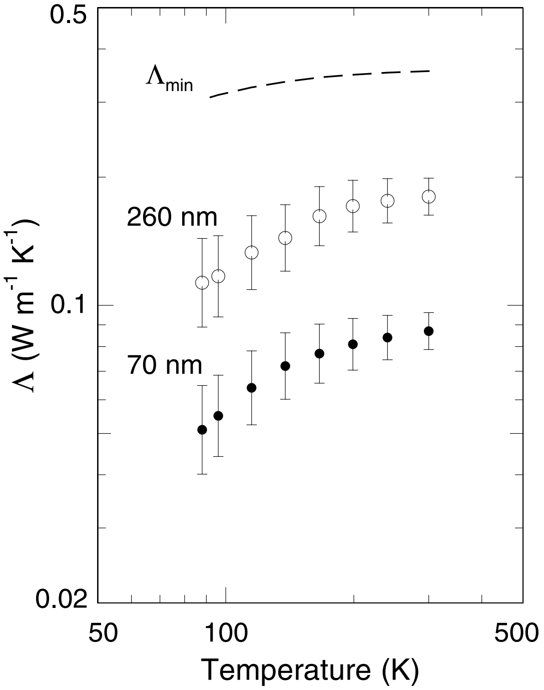

Figure 35. Summary of measured thermal conductivities of $MoSe_2$ films as a function of the measurement temperature. The samples were annealed at 625 ºC for 1 h prior to measurements. Each curve is labeled by the film thickness. The interrupted line marked Λ_{min} is the calculated minimum thermal conductivity for $MoSe_2$ films in the cross-plane direction.

In Figure 35 I compare the cross-plane thermal conductivity of annealed $MoSe_2$ films to the predicted minimum thermal conductivity calculated using longitudinal and transverse speeds of sound and the number density of atoms ($N = 4.96x10^{22}$ atoms cm^{-3}). I measured the longitudinal speed of sound in the cross-plane direction of nominal 260 nm thick films using picosecond acoustics: average value , $v_L = 2.0$ nm ps^{-1}. I estimated transverse speed of sound v_T=1.4 nm ps^{-1} from measurement of v_L and the literature ratio C_{44}/C_{33} for $NbSe_2$ and $TaSe_2$ [63]. The lowest thermal conductivity Λ measured at 300 K is $\Lambda = 0.087$ W m^{-1} K^{-1} for a 70 nm thick $MoSe_2$ film, a factor of 4 smaller than the predicted minimum thermal conductivity of $MoSe_2$. The conductivity of the thicker 260 nm film is almost two times larger, $\Lambda = 0.36$ W m^{-1} K^{-1} at 300 K.

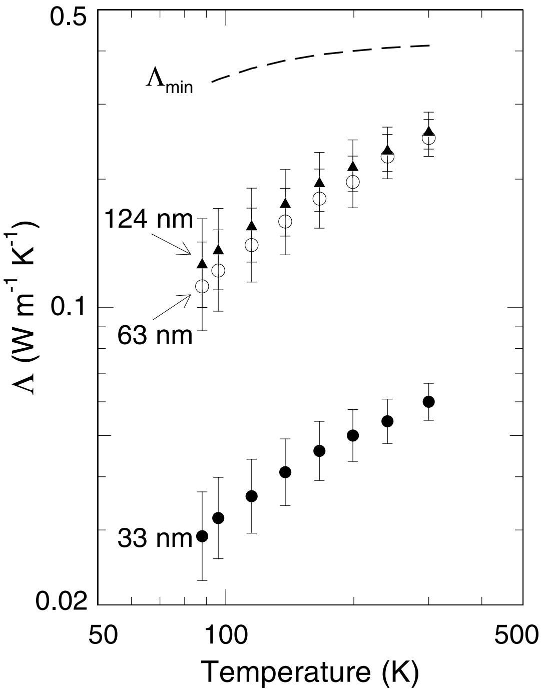

Figure 36. Summary of measured thermal conductivities of $NbSe_2$ films as a function of the measurement temperature. The samples were annealed at 400 ºC for 1 h prior to measurements. Each curve is labeled by the film thickness. The interrupted line marked Λ_{min} is the calculated minimum thermal conductivity for $NbSe_2$ films in the cross-plane direction. Samples were annealed at 400 ºC for 1 hour prior to measurements.

Figure 36 summarizes the thermal conductivity measurements on annealed $NbSe_2$ films. The lowest thermal conductivity Λ measured at 300 K is $\Lambda = 0.06$ W m^{-1} K^{-1} for a 33 nm thick $NbSe_2$ film, a factor of 7 smaller than the predicted minimum thermal conductivity of $NbSe_2$. I calculated Λ_{min} using number density of atoms N = 4.66x10^{22} atoms cm^{-3} and literature values [63] for the speeds of sound, v_L =2.55 nm ps^{-1} and v_T = 1.65 nm ps^{-1}. Thermal conductivities of thicker $NbSe_2$ films is significantly larger, Λ = 0.25 W m^{-1} K^{-1} at 300 K, yet still lower then estimated Λ_{min}.

$NbSe_2$ exhibits metallic behavior 19 with an electrical resistivity along the *c*-axis that is a factor of 30 larger then the electrical resistivity in the *a-b* plane [65]. I estimated the electronic contribution to the thermal conductivity of the $NbSe_2$ films from measurements of the in-plane electrical conductivity of films deposited on fused-quartz substrates. The $NbSe_2$ films were deposited using the same recipe as the ones formed on Si (100) substrates for the thermal conductivity measurements (TDTR measurements require high thermal conductivity substrates). Room temperature electrical measurements showed the $NbSe_2$ films have p-type conduction and the *a-b* plane average electrical conductivity is 1550 $(\text{ohm-cm})^{-1}$ for 30 nm films, and 3650 $(\text{ohm-cm})^{-1}$ for 60 nm films and 120 nm thick films. These values are a factor of 4.3 and respectively 1.8 times lower then the bulk [65, 66] *a-b* plane electrical conductivity for $NbSe_2$. I estimated the electronic component of the thermal conductivity Λ_e using the Wiedemann Franz law with a degenerate Lorenz number $L = \pi^2 (k_B/e)^2 / 3 = 2.45\text{x}10^{-8}\ V^2/K^2$ and *c*-axis electrical conductivity 0.03 times the *a-b* plane values. The *c*-axis $\Lambda_e = 0.04\ W\ m^{-1}\ K^{-1}$ for 30 nm $NbSe_2$ films, and $0.09\ W\ m^{-1}\ K^{-1}$ for 60 and 120 nm thick $NbSe_2$ films. Given the turbostratic microstructure of our thin film samples, I expect that the anisotropy of electrical conductivity will be significantly larger than in the bulk, and thus the electronic contribution to the *c*-axis thermal conductivity of $NbSe_2$ will be significantly smaller.

The data shown in Figure 28 and Figure 34 lead to the conclusion that the ultra-low thermal conductivities are produced by random-stacking of well-crystallized WSe_2 sheets. To test this idea, I used irradiation by energetic heavy ions to disrupt the crystalline order in the thin film samples (Figure 37). At the highest ion dose, $3\text{x}10^{15}$ ions cm^{-2} (10.5 DPA), I observed a factor of 5 increase in the thermal conductivity of the WSe_2 film (see Figure 38) and Λ approaches the value estimated for the amorphous WSe_2

(see Figure 34). This increase in thermal conductivity with ion beam damage is also unprecedented.

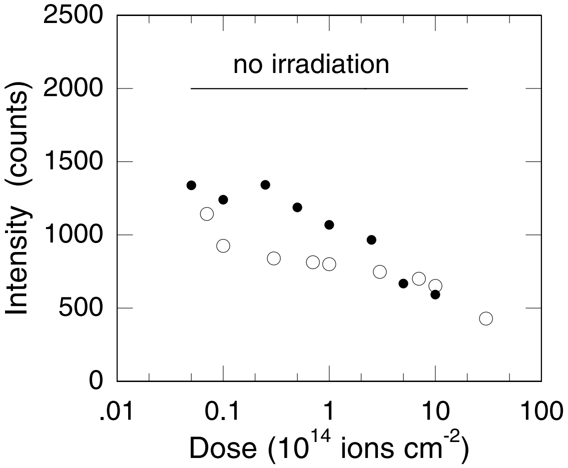

Figure 37. XRD intensity of the (002) peak as a function of ion bombardment dose for 26 nm thick film (open circles) and 100 nm film (filled circles – measured at University of Oregon) of WSe_2. The uninterrupted line marked "no irradiation" indicates the intensity of the (002) peak in the same film, not subjected to ion irradiation.

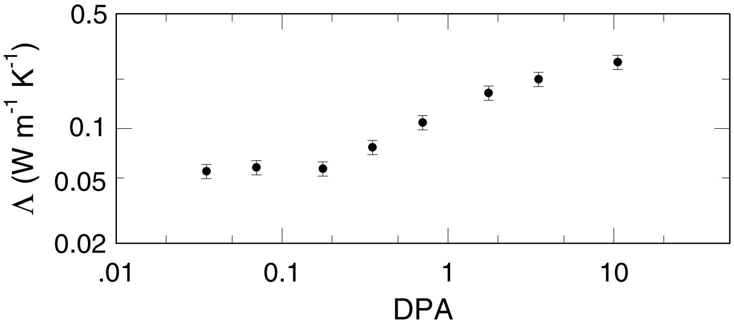

Figure 38. Thermal conductivity versus irradiation dose for WSe_2 films 26 nm thick. Samples were irradiated with 1 MeV Kr^+ ions to the dose indicated on the x-axis of the plot (in DPA units).

To gain further insight and confidence in the experimental results, molecular dynamics simulations on model structures were performed by Professor Keblinski and his group at Rensselaer Polytechnic Institute. The estimated value for thermal conductivity Λ is 0.06 W m^{-1} K^{-1} , with a 10% error bar. Given the approximate form of the potentials used in the computational work, the agreement between the measured and calculated thermal conductivities is better than expected. Nevertheless, the low thermal conductivity of the model structure suggests that the ultra-low thermal conductivity in layered, disordered crystals is a general phenomenon and not restricted to WSe_2. This conclusion is supported by the measurements on the $MoSe_2$ (Figure 35) and $NbSe_2$ (Figure 36) samples. I speculate at this time that the differences in Λ between the thinner and thicker disordered layered films are due to variations in the crystallographic order along the thickness of the films: annealing data (see Figure 31 to Figure 33) suggests the samples re-crystallize as a result of increased heat treatment temperatures, i.e., the crystalline coherence length is increasing. Also, electrical measurements data suggests the variations in electrical conductivity in the 30 nm and 60 and 120 nm films of $NbSe_2$ are caused by different electrical anisotropy ratios in the thin and thick films. These variations could be a result of different degrees of turbostratic disorder.

3.4 Conclusions

In summary, I found that the thermal conductivity of disordered, layered crystalline materials is significantly less than the predicted minimum thermal conductivity for the cross-plane direction and that the thermal conductivity increases when the layered structure is disrupted by ion bombardment. These results demonstrate that control of both order and disorder, i.e., the disordered stacking of well-ordered crystalline sheets of a layered crystal, can produce unexpected and dramatic reductions in thermal conductivity. Molecular dynamics simulations on model structures suggest and the experimental data concurs that the ultra-low thermal conductivity in layered, disordered crystals is a general phenomenon.

CHAPTER 4

THERMAL CONDUCTIVITY OF MISFIT LAYERED MATERIALS

Significant components of this chapter were published in “Low thermal conductivity in nanoscale layered materials synthesized by the method of modulated elemental reactants”, Journal of Applied Physics 104, 033533 (2008). I collaborated with Professor David Johnson, Mr. Qiyin Lin and Mr. Colby Heideman at University of Oregon for sample deposition and structural characterization. I measured the thickness, composition, thermal and elastic properties of the samples described in this chapter.

4.1 Introduction

In the previous section I showed that ultralow thermal conductivity is a general property of layered disordered crystalline metal dichalcogenides, and possibly common to all layered disordered materials. Literature reports have also demonstrated that superlattices of semiconductors can have thermal conductivities less than the conductivity of the corresponding alloy [67] ; and that nanoscale multilayers of oxides and metals can have thermal conductivities smaller than the conductivity of typical refractory thermal barriers [58]. With these ideas in mind I set up to explore ways to produce even lower thermal conductivity in nanoscale multilayer films in which the layers have different compositions and crystal structures.

One class of materials that fits the profile is that of the misfit-layered compounds. The general chemical formula of these compounds is $[(MX)_m (TX_2)_n]$ where X = S and

Se, M = Sn, Pb, Sb, Bi, and rare earth metals, and T= Ti, V, Cr, Nb, Ta and other transition metals. These structure of these compounds consist of alternating distorted rock salt layers with dichalcogenide layers [68, 69, 70]. The distortion in the rock salt results from the coordination of the metal in the rock-salt layer by the Se in the dichalcogenide layer (i.e., Pb by Se from the TSe_2 layer) [71]. The values m and n represent the number of rock salt bilayers and the number of Se-T-Se planes in the unit cell, respectively. Charge transfer is generally accepted [72] as the stabilizing mechanism for the misfit structure over a physical mixture of the components.

This section shows the results of my investigation of the thermal conductivity of thin film samples of misfit-layer dichalcogenide films $[(PbSe)_m (TSe_2)_n]_i$ (T = W, Mo or Nb, m = 1-5, n = 1-5) synthesized by the modulated elemental reactants method.

4.2 Experimental Details

Thin films of nanoscale layered materials were synthesized using the modulated elemental reactants (MER) method. Pb, W, Nb and Mo were evaporated from electron-beam sources; Se was evaporated from effusion cells. To synthesize misfit-layer chalcogenides with layer formula $[(PbSe)_m (TSe_2)_n]_i$ (X = W, Nb or Mo, m = 1-5, n = 1-5, i = 10-40) , we started by depositing onto unheated Si(001) wafers m bilayers of Pb and Se with 1:1 atomic ratio followed by n bilayers of X and Se (X = W, Nb or Mo) with 1:2 atomic ratio. The $m+n$ sequence was repeated i times and the as-deposited films were annealed for 1 hour at 400 °C in dry N_2. The total thickness of annealed $[(PbSe)_m (MoSe_2)_n]_i$ films varied between 40 and 60 nm, except for sample $[(PbSe)_3 (MoSe_2)_3]_i$ which was 115 nm thick. The total thickness of the annealed $[(PbSe)_m (WSe_2)_n]_i$ films varied from 20 to 60 nm. The $[(PbSe)_m (NbSe_2)_n]_i$ films were 50 nm nominally thick.

For comparison purposes, a 260 nm thick PbSe sample was synthesized by the same approach.

The stoichiometry and oxygen contamination of the films were determined at University of Oregon by electron-probe micro-analysis (EPMA). The EPMA data was refined using the STRATAGem software package. Oxygen content was on average 5 at.%.

The crystalline quality, crystallographic orientation, and thickness of the films were evaluated by x-ray diffraction (XRD) and x-ray reflectivity (XRR) using a Bruker D8 Discover diffractometer with Cu $K_{\alpha 1}$ radiation. Thickness of the films was derived from the Kiessig fringes in low angle ($2\theta < 10$ degrees) XRR scans. The period of the repeat unit was determined from the position of the satellites of the high-angle (0 0 L) diffraction peaks [73].

Thermal conductivity was measured at room temperature using time-domain thermoreflectance (TDTR). Prior to the measurements, I coated the samples with a transducer layer of Al, 80-85 nm thick, using dc magnetron sputtering. I used a $1/e^2$ radius of the focused spots of 7.5 microns and the total incident laser power was typically 10 mW. The steady-state temperature rise was estimated at 3 - 9 K. The differences in reflected probe intensity caused by the heating due to the pump pulses were extracted with a rf lock-in amplifier synchronized to the modulation frequency of the pump ($f = 9.8$ MHz).

I determined the thermal conductivity of the samples by comparing calculations made with a thermal model to the time dependence of the in-phase signal V_{in} of the rf lock-in normalized by the out-of-phase signal V_{out}. The thermal conductivity of the Al layer was estimated using the Wiedemann-Franz law and 4-point probe measurements of the in-plane electrical resistivity; the thickness of the Al layer was measured by picosecond acoustics. The heat capacity of the Al layer [31], and heat capacity [32] and thermal conductivity [33] of the Si substrate are taken from literature values. The heat capacity of each sample layer is a volume weighted average of the heat capacities at 300 K of the individual components: WSe_2 [38] (1.95 J cm^{-3} K^{-1}), $MoSe_2$ [39] (1.94 J cm^{-3} K^{-1}), $NbSe_2$ [40] (1.93 J cm^{-3} K^{-1}) and PbSe [41] (1.44 J cm^{-3} K^{-1}). The overall uncertainty in measuring the thermal conductivity was estimated at 10%.

I measured the cross-plane longitudinal speed of sound v_L in the films using picosecond acoustics; v_L is determined from the sample thickness measured by x-ray reflectivity and the difference in the arrival times of acoustic echoes reflected from the Al / sample and sample / substrate interfaces.

4.3 Results and Discussion

X-ray diffraction scans of as-deposited films (data not shown) contain weak and broad high angle (00L) Bragg peaks corresponding to the target chemical compounds. The peaks become sharper with increasing annealing temperature indicating the formation of highly textured structures with layers aligned parallel to the surface of the substrate. The period of the repeat unit extracted from the (00L) Bragg peaks in the high angle XRD scans are in good agreement with the period of repeat unit calculated using the lattice constants and the target compositions and structures for each sample (see for example Figure 39).

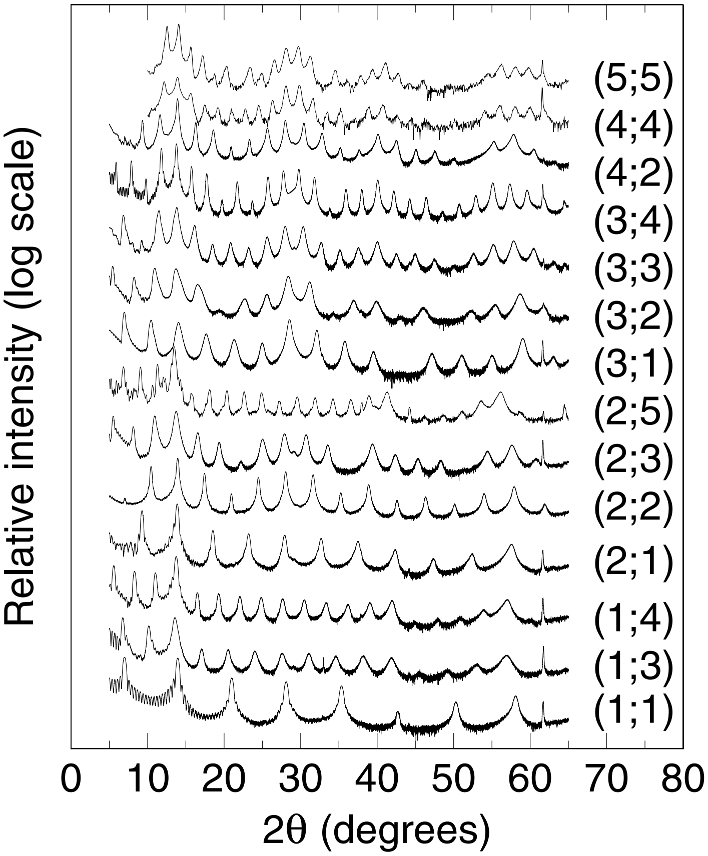

Figure 39. Diffraction patterns of the $(PbSe)_m(WSe_2)_n$ compounds after annealing at 400 °C for 1 hour. The structures calculated for each compound show a regular increase in the *c*-axis of the unit cell.

I analyzed the stoichiometry and areal density of the sample films using RBS (see Figure 40). The conversion factors used to convert channel to energy in Figure 40 are: (PbSe) $(MoSe_2)$ – calibration offset 135 keV and energy per channel 1.803 eV/ch; $(PbSe)_5$ $(WSe_2)_5$ – calibration offset 140 keV and energy per channel 1.852 eV/ch; $(PbSe)_2$ $(NbSe_2)_2$ – calibration offset 141 keV and energy per channel 1.782 eV/ch. The quadratic term was null for all measurements.

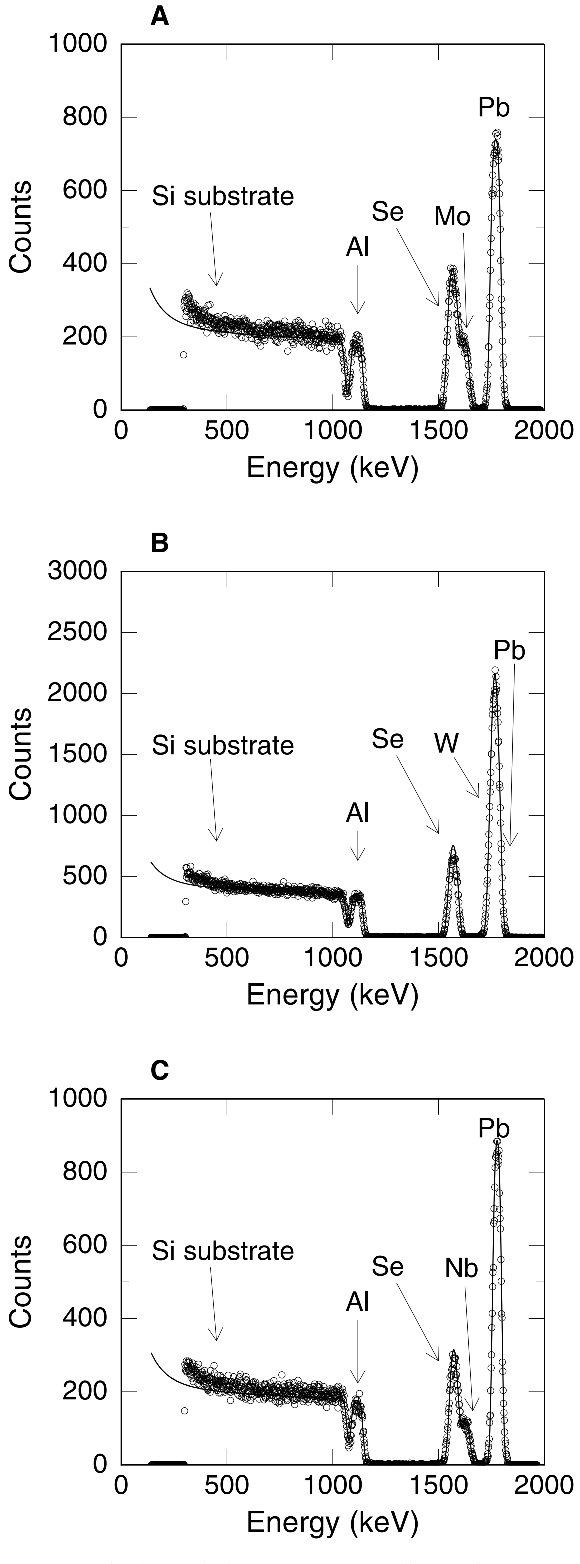

Figure 40. RBS spectra (open circles) and the SIMNRA fit (uninterrupted line) for (A) 53 nm thick (PbSe) ($MoSe_2$) film; (B) 48 nm thick $(PbSe)_5$ $(WSe_2)_5$ film; (C) 49 nm thick $(PbSe)_2$ $(NbSe_2)_2$ film.

The ratio Pb : X : Se (X = W, Mo or Nb) is within 5% of those predicted by the model crystalline structure for [$(PbSe)_m$ $(WSe_2)_n$] and within 3% for [$(PbSe)_m$ $(MoSe_2)_n$] and [$(PbSe)_m$ $(NbSe_2)_n$] misfit layer samples. Average mass density of the sample films agree within 5% with the values estimated by XRR and within 3% with those predicted by the crystalline structure model of each compound.

As shown in Figure 41, Figure 42, and Figure 43, we have not succeeded in creating materials with thermal conductivity Λ below what I previously measured for single component WSe_2 films, $\Lambda = 0.05$ W m^{-1} K^{-1}. Thermal conductivity is reasonably well correlated with the composition of the film, i.e., the PbSe content, but it does not display a significant correlation with the density of interfaces, i.e., the period of the multilayer.

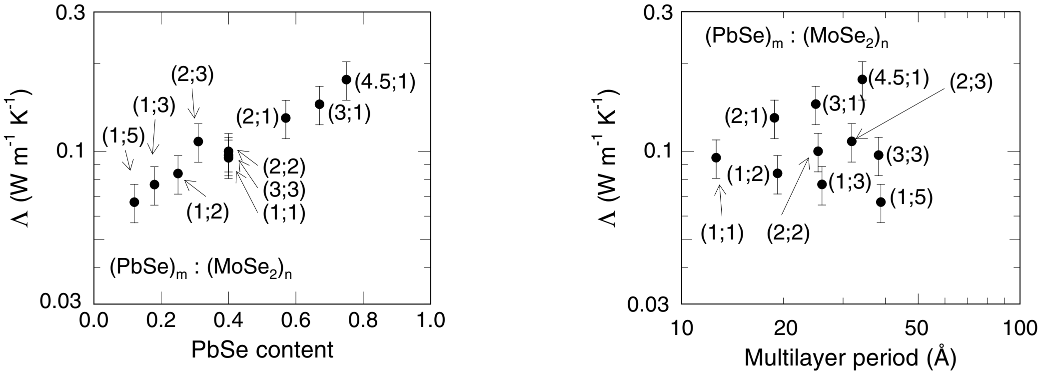

(A)

(B)

Figure 41. Cross-plane thermal conductivity of $(PbSe)_m$ $(MoSe_2)_n$ films. Data are plotted as a function of (A) PbSe atomic fraction (calculated as $2m/(2m+3n)$); and (B) thickness of the misfit layer repeat unit. Each data point is labeled by a $(m;n)$ index for the film where m is the number of PbSe bilayers and n is the number of $MoSe_2$ sheets in the repeat unit.

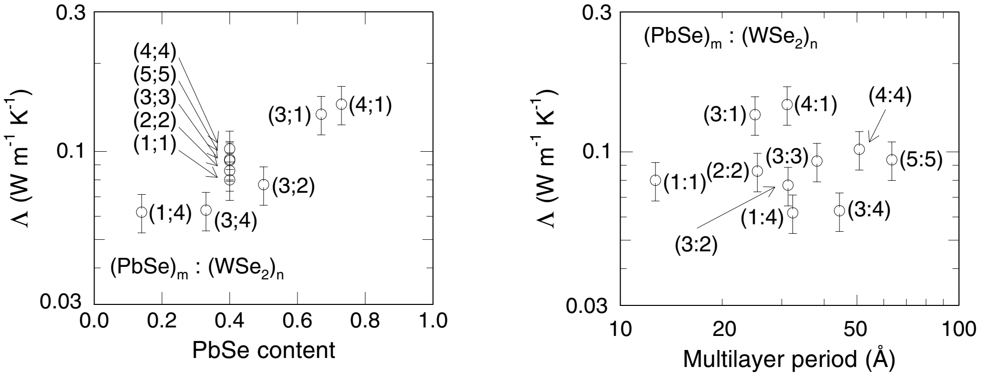

(A) **(B)**

Figure 42. Cross-plane thermal conductivity of $(PbSe)_m$ $(WSe_2)_n$ films. Data are plotted as a function of (A) PbSe atomic fraction (calculated as $2m/(2m+3n)$); and (B) thickness of the misfit layer repeat unit. Each data point is labeled by a (m;n) index for the film where m is the number of PbSe bilayers and n is the number of WSe_2 sheets in the repeat unit.

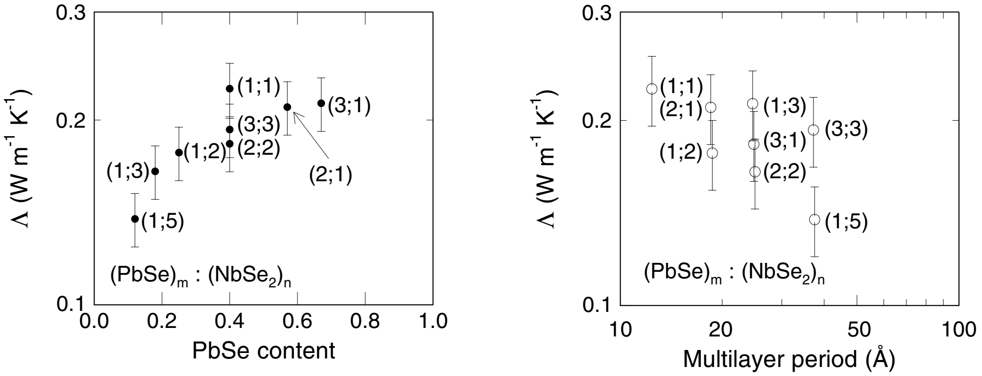

(A) **(B)**

Figure 43. Cross-plane thermal conductivity of $(PbSe)_m$ $(NbSe_2)_n$ films. Data are plotted as a function of (A) PbSe atomic fraction (calculated as $2m/(2m+3n)$); and (B) thickness of the misfit layer repeat unit. Each data point is labeled by a (m;n) index for the film where m is the number of PbSe bilayers and n is the number of $NbSe_2$ sheets in the repeat unit.

The lowest thermal conductivities are 0.07 W m^{-1} K^{-1} for $(PbSe)_1$ $(MoSe_2)_5$, 0.06 W m^{-1} K^{-1} for $(PbSe)_1$ $(WSe_2)_4$, and 0.14 W m^{-1} K^{-1} for $(PbSe)_1$ $(NbSe_2)_5$. These values are approximately a factor of 5 and respectively 3 smaller than the minimum thermal conductivity of PbSe Λ_{min} = 0.38 W m^{-1} K^{-1} calculated using the speeds of sound [74]

(v_T = 1.4 nm/ps and v_L = 3.9 nm/ps) and mass atomic density of 8.3 g cm^{-3} of PbSe. These values are also approximately a factor of 4 and respectively 2 smaller than the minimum thermal conductivity of WSe_2 $\Lambda_{min} = 0.29$ W m^{-1} K^{-1} calculated in Chapter 3.

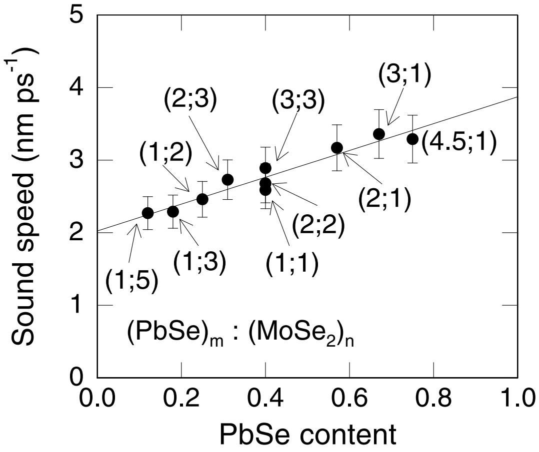

Figure 44. Longitudinal speed of sound of $(PbSe)_m$ $(MoSe_2)_n$ films as a function of the PbSe atomic fraction (calculated as $2m/(2m+3n)$). Each data point is labeled by a (m;n) index for the film, where m is the number of PbSe bilayers and n is the number of $MoSe_2$ sheets in the repeat unit. The solid line is a linear extrapolation of the data used to extract the longitudinal speed of sound for pure $MoSe_2$ and PbSe.

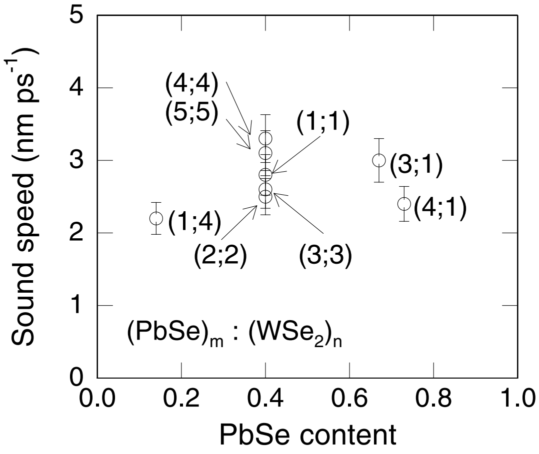

Figure 45. Longitudinal speed of sound of $(PbSe)_m$ $(WSe_2)_n$ films as a function of the PbSe atomic fraction (calculated as $2m/(2m+3n)$). Each data point is labeled by a (m;n) index for the film, where m is the number of PbSe bilayers and n is the number of WSe_2 sheets in the repeat unit.

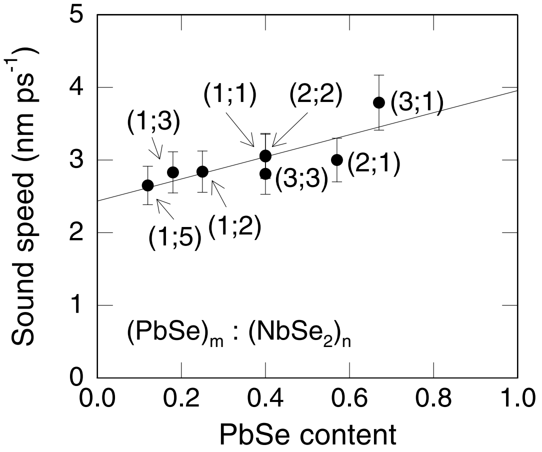

Figure 46. Longitudinal speed of sound of $(PbSe)_m$ $(NbSe_2)_n$ films as a function of the PbSe atomic fraction (calculated as $2m/(2m+3n)$). Each data point is labeled by a $(m;n)$ index for the film, where m is the number of PbSe bilayers and n is the number of $NbSe_2$ sheets in the repeat unit. The solid line is a linear extrapolation of the data used to extract the longitudinal speed of sound for pure $NbSe_2$ and PbSe.

The cross-plane longitudinal speeds of sound v_L of the misfit-layer films (Figure 44, Figure 45 and Figure 46) indicate a softening of the lattice with decreasing PbSe content; this behavior is most clearly shown in the data for $(PbSe)_m$ $(MoSe_2)_n$ and $(PbSe)_m$ $(NbSe_2)_n$ films, see Figure 44 and Figure 46. As was the case with the data for Λ, the density of interfaces does not appear to have a significant influence on v_L. A linear extrapolation of these data to pure $MoSe_2$, $NbSe_2$ and PbSe gives elastic constants of C_{33}= 28 GPa, C_{33}= 42 GPa and C_{11}= 124 GPa, respectively. The results are similar to literature values for longitudinal elastic constant of PbSe [74] (C_{11}=124 GPa) and $NbSe_2$ [63] (C_{33}= 42 GPa) and similar to the longitudinal elastic constant for WSe_2 (C_{33}=25.6 GPa), measured in chapter 3.

4.4 Conclusions

Using nanoscale multilayers prepared by modulated elemental reactants method, I have demonstrated a large variety of nanostructured materials with thermal conductivities significantly below the predicted minimum thermal conductivity of the component materials used to create the multilayer. I was not successful, however, in producing thermal conductivities below the ultralow values I reported in single component WSe_2 films. For multilayer materials with similar composition, changes in the density of interfaces—or equivalently, changes in the thicknesses of the individual layers—do not produce significant changes in the thermal conductivity. This null result (the relative insensitivity of the data to the density of interfaces) is somewhat surprising since the finite thermal conductance of interfaces between different materials is usually thought to play an important role in the reduction of thermal conductivity in multilayers and superlattices. Apparently, the interface thermal conductance is not a significant factor for heat transfer in the multilayer materials reported here; and the thermal conductivity is instead controlled by the unusual thermal properties of the disordered layered crystals such as WSe_2 that are included in the multilayer.

The origin of ultra-low thermal conductivity of layered disordered WSe_2 films was recently studied [75] using molecular dynamics simulations and vibrational mode analysis on model structures. This study shows that the ultra-low thermal conductivity can be attributed to the strong anisotropy in the elastic constants of the materials due to weak interplanar Van der Waals bonding. The anisotropy suppresses the density of vibrational modes with wave-vectors that have components in the cross-plane direction of the samples, so there are fewer phonon modes carrying heat in that direction than is assumed in the model of the minimum thermal conductivity. This conclusion of is consistent with our experimental results: in the misfit layer films, the cross-plane thermal conductivity decreases with increasing content of the main source of anisotropy in the sample, the layered chalcogenide; and the thermal conductivity is largely unaffected by variations in superlattice period.

CHAPTER 5

THERMAL CONDUCTIVITY OF NANOSCALE LAYERED MATERIALS

Significant components of this chapter were published in "Low thermal conductivity in nanoscale layered materials synthesized by the method of modulated elemental reactants", Journal of Applied Physics 104, 033533 (2008), and "Lower limit to the lattice thermal conductivity of nanostructured Bi_2Te_3-based materials", Journal of Applied Physics 106, 073503 (2009). I collaborated with Professor David Johnson and Dr. Clay Mortensen from University of Oregon for sample deposition and structural characterization. I measured the thermal and elastic properties of the samples described in this chapter. I thank Mr. Yee Kan Koh for his help in implementing the Debye – Callaway model used in this chapter.

5.1 Introduction

In the previous section I showed that by incorporating disordered layered materials in multilayer films, we can control the thermal conductivity Λ of the multilayer by controlling the amount of disordered material rather then the density of abrupt interfaces. This observation has motivated me to explore how I might extend this behavior into classes of materials that are known to have high power factors for thermoelectric energy conversion, e.g., Bi_2Te_3 and Bi_2Te_3/Sb_2Te_3 multilayers [76].

Recently [77, 78], nanostructured Bi_2Te_3 prepared by ball-milling and spark-plasma-sintering have been demonstrated with significantly enhanced efficiency in comparison to materials prepared by traditional methods of powder processing. The improved efficiency can be mostly attributed to a reduction in thermal conductivity created by scattering of phonons at the boundaries between nanoscale grains. These observations raise the question of how small of grains are needed to significantly reduce the lattice thermal conductivity and ultimately what is the lower limit to the lattice thermal conductivity of Bi_2Te_3-based thermoelectric materials.

To help answer these questions, we prepared a variety of thin films of Bi_2Te_3, related alloys, and multilayers with well-controlled structure on nanometer length scales. Specifically, we introduce disordered layers of $TiTe_2$ in multilayers to create strong phonon scattering on well-defined length scales of only a few nanometers.

Bismuth telluride [79] (Bi_2Te_3) and antimony telluride [80] (Sb_2Te_3) have rhombohedral crystal structures with one chemical formula per unit cell. The most often used description is the pseudo-hexagonal unit cell obtained by transformation of axes and containing three chemical formulae per unit cell with lattice parameters [81] : Bi_2Te_3 a = 4.4 Å, c = 30.5 Å; Sb_2Te_3 a = 4.3 Å, c = 30.4 Å. The hexagonal cell is formed by stacking of layers of like-atoms perpendicular to the c-axis and following the sequence (called quintet) Te-X-Te-X-Te (X = Bi or Sb); each quintet is bonded to the next by Te-Te bonds and longer-ranged electrostatic [82, 83] interactions. Titanium telluride ($TiTe_2$) has a hexagonal crystal structure [84] with one formula unit per unit cell (a = 3.8 Å, c = 6.5 Å). In this structure, one sheet is composed of a hexagonal plane of Ti atoms bonded to two Te layers by strong covalent–ionic bonds and each two-dimensional $TiTe_2$ sheet is bonded to adjacent sheets by weak Van der Waals forces.

This section shows the results of my investigation of the thermal conductivity of thin film samples of Bi_2Te_3 and Bi_2Te_3 – based materials. First, I looked at single layer homogeneous Bi_2Te_3, Sb_2Te_3 and multilayer $[(TiTe_2)_3\ (Bi_2Te_3)_m\ (TiTe_2)_3\ (Sb_2Te_3)_n]_i$ (m = 1-5, n = 1-5) samples to gauge the effects of superlattice structures on the thermal conductivity of our films. Second, thin films of alloy $(Bi_{0.5}Sb_{0.5})_2Te_3$, multilayer $(Bi_2Te_3)_m(TiTe_2)_n$ (m = 2-6, n=2-6) and multilayer alloy $[(Bi_xSb_{1-x})_2Te_3]_m(TiTe_2)_n$ were synthesized to optimize lowering the lattice thermal conductivity by small grains, alloy mix and the introduction of disordered layers in the structure .

5.2 Experimental Details

Multilayer thin films of nanoscale materials were synthesized using the modulated elemental reactants (MER) method. The films were deposited onto polished Si (100) oriented substrates. Bismuth, antimony and tellurium were deposited using effusion cells and titanium was deposited with an electron beam source.

To start, homogenous Bi_2Te_3 and Sb_2Te_3 films were prepared by depositing alternating layers of M (M = Bi or Sb) and Te with a 2:3 atomic ratio, each bilayer having a thickness of 10.1 Å. Homogenous $TiTe_2$ films were prepared by depositing alternating layers of Ti and Te with a 1:2 atomic ratio, each bilayer having a thickness of 6.5 Å. After annealing, each Bi/Te bilayer formed a Te-Bi-Te-Bi-Te layers quintet, one-third of a hexagonal Bi_2Te_3 unit cell; each Ti/Te layer resulted in a Ti-Te-Ti sheet. Annealing was done in a dry N_2 environment (< 0.4 ppm O_2). The single-component Bi_2Te_3 films were annealed at 100, 150, 200, 250, 300 or 350 °C for 15 minutes and at 400 °C for 1 minute. The single-component Sb_2Te_3 films were annealed in dry N_2 atmosphere at 100, 150, 200, 250 and 300 °C for 15 minutes, at 350 °C for 2 minutes, or at 400 °C for 1 minute. The single-component $TiTe_2$ films were annealed in dry N_2 atmosphere at 150, 250 and 300 °C for 5 and 30 minutes. Bi_2Te_3 and Sb_2Te_3 films single-component films were 100 nm nominally thick; $TiTe_2$ films were 50 nm nominally thick.

Three-component multilayer films with layer formulas $[(TiTe_2)_3\ (Bi_2Te_3)_m\ (TiTe_2)_3\ (Sb_2Te_3)_n]_i$ (m = 1-5, n = 1-5, i = 5-7) were synthesized by depositing a sequence of single elements: three bilayers of Ti and Te with 1:2 atomic ratio, followed by m bilayers of Bi and Te with 2:3 atomic ratio, followed by another sequence of three bilayers of Ti and Te with 1:2 atomic ratio, and finally n sequential bilayers of Sb and Te with 2:3 atomic ratio. The sequence was repeated i times and then the films were annealed for 5 minutes at 250 °C in dry N_2 atmosphere. After annealing, the nominal thickness of the 3-component films was 55 nm.

Three different series of $[(Bi_2Te_3)_m\ (TiTe_2)_n]$ (m, n = 2-6) multilayer films were prepared: in the first one, the repeat unit contained m = 3 bilayers of Bi and Te with 2:3 atomic ratio, followed by n = 2 - 6 bilayers of Ti and Te with 1:2 atomic ratio; in the second series, the repeat unit contained m = 2-6 bilayers of Bi and Te with 2:3 atomic ratio, followed by n = 3 bilayers of Ti and Te with 1:2 atomic ratio; the third series consisted of multiples of the repeat unit containing equal number of Bi/Te followed by Ti/Te bilayers with $m = n$ = 2, 5, and 6. After annealing at 300 °C for 30 minutes, the films were 50-100 nm thick.

The alloy and multilayer alloy films were prepared by depositing alternating bilayers of Bi/Te, Sb/Te and Ti/Te. Films with chemical composition $(Bi_{0.5}Sb_{0.5})_2Te_3$ were deposited and then annealed in sealed quartz ampoules evacuated to $1x10^{-6}$ Torr in the presence of Te-rich Bi_2Te_3 powder. The films were subsequently annealed at 150 °C for 30 min, at 250 °C for 10 min, or at 300 °C for 4 and 8 min and after annealing were ≈60 nm thick. Films with chemical composition $[(Bi_xSb_{1-x})_2Te_3]_m (TiTe_2)_n$ ($x = 0.55$ +/- 0.09, $m = 2$-4, $n = 3$ and 6) were deposited using the same recipe but annealed in a dry N_2 atmosphere at 250 °C. After annealing, the films had a thickness between 40 and 60 nm.

The stoichiometry and oxygen contamination of the films were determined by electron-probe micro-analysis (EPMA). The EPMA data were refined using the STRATAGEM software package. Oxygen content was on average 7 at.% in the 3-component films and 3 at.% in the 2-component films.

X-ray diffraction (XRD) and x-ray reflectivity (XRR) were employed to determine the phase-formation, grain-size, film thickness, multilayer-period and the crystallographic orientation of the as-deposited and annealed samples. The x-ray studies were performed using Cu $K\alpha_1$ radiation source with a Goebel mirror to collimate the beam. Thickness of the films was evaluated from the Kiessig fringes of low angle XRR scans. The period of the multilayers was determined from the position of superlattice Bragg diffraction maxima in the high angle XRD data. The grain size was calculated using the Scherrer equation after accounting for the contribution of instrumental broadening, $\Delta (2\theta) \approx 0.05°$, to the width of the (003) diffraction peak.

Grazing incidence in-plane x-ray diffraction (GIIXRD) and high-angle x-ray diffraction (HAXRD) data of the as-deposited alloy and multilayer alloy samples indicate the incipient formation of alloy composition with nanometer size grains. Subsequent annealing promoted grain growth of the respective alloy composition, as noted from the narrowing of the diffraction maxima. The $(Bi_{0.5}Sb_{0.5})_2Te_3$ alloy films are highly textured in the [0 0 L] crystallographic direction. Post deposition annealing of the multilayer

$[(Bi_2Te_3)_m (TiTe_2)_n]$ samples results in superlattice formation as determined from the presence of superlattice Bragg diffraction past the 30th order corresponding to the superlattice period.

X-ray diffraction studies of the $[(Bi_xSb_{1-x})_2Te_3]_m (TiTe_2)_n$ films showed the formation of high quality multilayers with precise stacking of the *a-b* planes of the superlattice relative to the substrate. Bragg diffraction maxima were observed past the 50th order, indicating the high quality of the alloy multilayer. Diffraction data obtained using an in-plane geometry revealed diffraction corresponding to $TiTe_2$ and $(Bi,Sb)_2Te_3$ with no diffraction observed corresponding to either Bi_2Te_3 or Sb_2Te_3, confirming the alloy nature of the superlattices.

I measured thermal conductivity of the samples at room temperature using time-domain thermoreflectance (TDTR). Prior to the measurements, I coated the samples with a transducer layer of Al, 80-85 nm thick, using dc magnetron sputtering. I used a $1/e^2$ radius of the focused spots of 7.5 microns and the total incident laser power was typically 20 mW. The steady-state temperature rise was estimated at 2 - 5 K. The differences in reflected probe intensity caused by the heating due to the pump pulses are extracted with a rf lock-in amplifier synchronized to the modulation frequency of the pump (f = 9.8 MHz).

I determined the thermal conductivity of the sample by comparing calculations made with a thermal model to the time dependence of the in-phase signal V_{in} of the rf lock-in normalized by the out-of-phase signal V_{out}. The thermal conductivity of the Al layer was estimated using the Wiedemann-Franz law and 4-point probe measurements of the in-plane electrical resistivity; the thickness of the Al layer was measured by picosecond acoustics. The heat capacity of the Al layer [31], and heat capacity [32] and thermal conductivity [33] of the Si substrate are taken from literature values. The heat capacity of each sample layer is a volume weighted average of the heat capacities of the individual components: Bi_2Te_3 [35], Sb_2Te_3 [36] and $TiTe_2$ [37] for the 2- and 3-component samples. The overall uncertainty in measuring the thermal conductivity was estimated at 10%. I measured the cross-plane longitudinal speed of sound v_L in the films using picosecond acoustics; v_L is determined from the sample thickness measured by x-ray reflectivity and the difference in the arrival times of acoustic echoes reflected from the Al / sample and sample / substrate interfaces.

5.3 Results and Discussion

Structural characterization of he samples was obtained using synchrotron x-ray diffraction at beam line 33-ID-D at the Argonne Lab Advanced Photon Source. The degree of turbostratic disorder in the annealed samples was evaluated by scanning the diffraction intensity through reciprocal space where the (1 0 L) reflection intersected the Ewald sphere. These studies revealed that $TiTe_2$ exhibits turbostratic disorder; i.e., the annealed films have a disordered layered structure with precise stacking of the *a-b* planes relative to the substrate and small coherence lengths, 6 nm in the in-plane and 8 nm in the out-of-plane directions.

Temperature dependence of thermal conductivity exhibits a behavior similar to the disordered layered chalcogenides previously described in chapter 3 (Figure 47). To calculate the minimum thermal conductivity Λ_{min} for $TiTe_2$, I measured cross-plane longitudinal speed of sound $v_L = 1.7$ nm ps^{-1} using picosecond acoustics. Using v_L and a mass density of 6.27 g cm^{-3}, gives the elastic constant $C_{33} = 18$ GPa, 2 - 3 times less then literature values for $TiSe_2$ [85] (C_{33} = 39 GPa) and TiS_2 [86] (C_{33} = 55 GPa). I estimated cross-plane transversal speed of sound v_T = 1 nm ps^{-1} from the measurement of v_L and the literature ratio C_{44}/C_{33} for $TiSe_2$ and TiS_2.

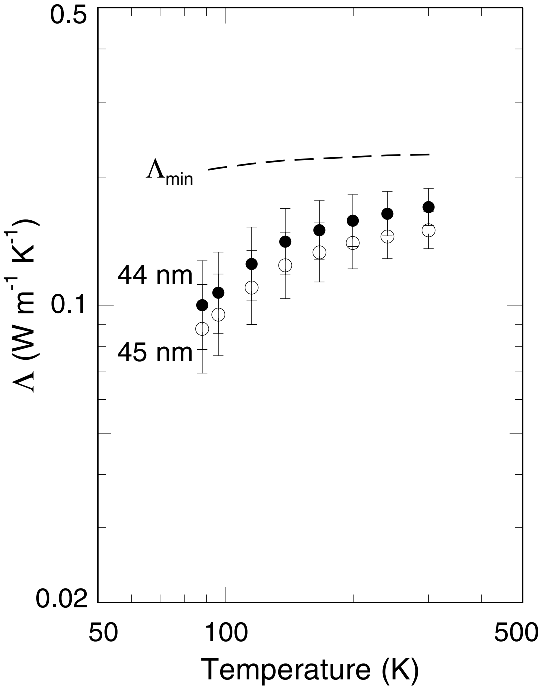

Figure 47. Summary of measured thermal conductivities of $TiTe_2$ films as a function of the measurement temperature. The samples were annealed at 300 ºC for 5 minutes prior to measurements. Each curve is labeled by the film thickness. The interrupted line marked Λ_{min} is the calculated minimum thermal conductivity for $TiTe_2$ films in the cross-plane direction.

Typically, annealing of materials at elevated temperature reduces the density of crystalline defects and leads to an increase in thermal conductivity. The thermal conductivity Λ of single-component Bi_2Te_3 and Sb_2Te_3 films follows this expected behavior up to an annealing temperature of approximately 200 ºC, see Figure 48. For an annealing temperature of 250 ºC, the thermal conductivity Λ of two-component films is a factor of 2 smaller than Λ of single-component films and the thermal conductivity of three-component films is a factor of 4 smaller than Λ of single-component films.

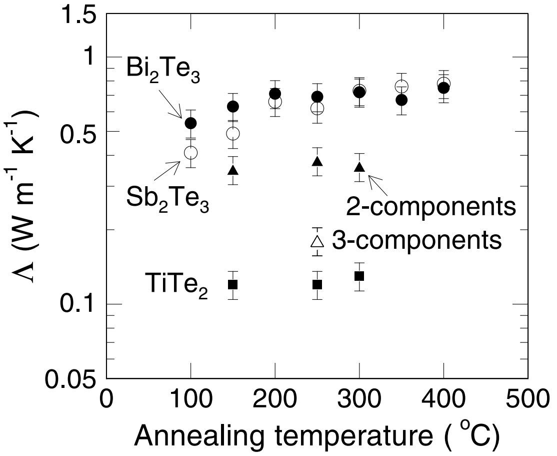

Figure 48. Cross-plane thermal conductivity of films based on Bi_2Te_3 and Sb_2Te_3 as a function of annealing temperature: 2-component Bi_2Te_3 / Sb_2Te_3 multilayers (filled triangles); 3-component Bi_2Te_3 / $TiTe_2$ / Sb_2Te_3 multilayers (open triangle); single-component Sb_2Te_3 (open circles); single-component Bi_2Te_3 (filled circles); and single-component $TiTe_2$ (filled squares). The data point for the 3-component film is the average of the thermal conductivities for several structures, see also Figure 49.

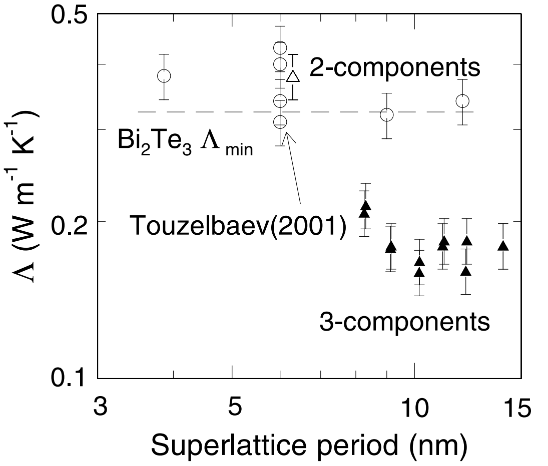

Figure 49. Cross-plane thermal conductivity of 3-component Bi_2Te_3 / $TiTe_2$ / Sb_2Te_3 films (closed triangle) and 2-component Bi_2Te_3 / Sb_2Te_3 films (open triangle) annealed at 250 °C. Open circles are thermal conductivities for Bi_2Te_3 / Sb2Te3 superlattices from Reference 87. Minimum thermal conductivity for Bi_2Te_3 (dashed line) is included for comparison.

The data for two-component Bi_2Te_3 / Sb_2Te_3 films are in good agreement with prior work [87] (see Figure 49) on the thermal conductivity of Bi_2Te_3 / Sb_2Te_3 multilayers prepared by chemical vapor deposition. Also included in Figure 49 is the predicted minimum thermal conductivity Λ_{min} for Bi_2Te_3 calculated using the cross-plane speeds of sound and the number density of atoms ($N = 2.96 \times 10^{22}$ atoms cm^{-3}). I measured the longitudinal speed of sound for homogeneous Bi_2Te_3 films and the value ($v_L = 2.5$ nm ps^{-1}) coincides with that estimated from reference [88] elastic constants ($C_{33} = 48$ GPa). I estimated the transverse ($v_T = 1.9$ nm ps^{-1}) speed of sound from literature values [89] for the elastic constants ($C_{44} = 27$ GPa) and the mass density 7.9 g cm^{-3}. The thermal conductivity for 3-component films is independent of the period of the multilayer and the average Λ (0.18 W m^{-1} K^{-1}) is two times lower than Λ_{min} of Bi_2Te_3. The low Λ of the 3-component films cannot be explained by a softening of the lattice. The average value of the longitudinal speed of sound in the 3-component films (2.45 nm ps^{-1}) is close to that measured for single-component Bi_2Te_3 (2.48 nm ps^{-1}) and Sb_2Te_3 (2.93 nm ps^{-1}) films annealed at the same temperature, 250 °C, see Figure 50.

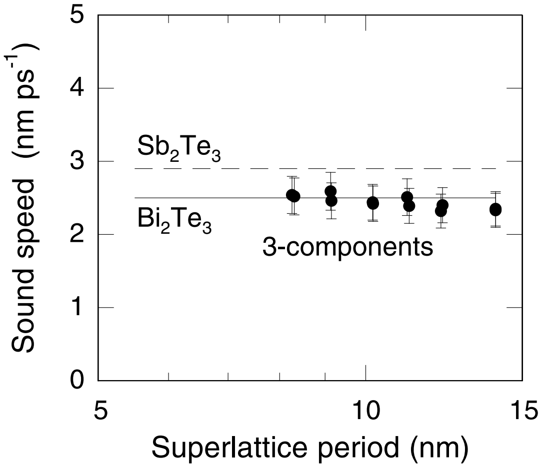

Figure 50. Longitudinal speed of sound for 3-component Bi_2Te_3 / $TiTe_2$ / Sb_2Te_3 films (closed circles) plotted as a function of superlattice period. Speed of sound in single-component Sb_2Te_3 and Bi_2Te_3 films (solid and dashed lines) are shown for comparison.

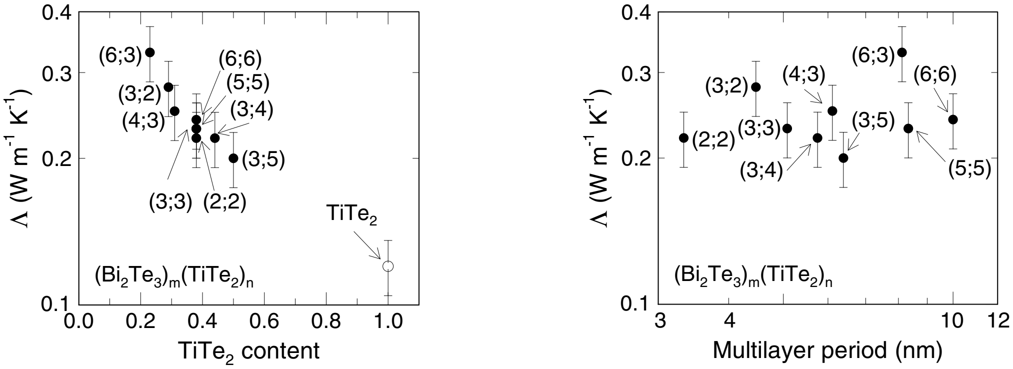

(A) **(B)**

Figure 51. Cross-plane thermal conductivity of $[(Bi_2Te_3)_m(TiTe_2)_n]$ (m = 2-6, n=2-6) films. Data are plotted as a function of (A) $TiTe_2$ atomic fraction (calculated as $3n/(5m+3n)$); and (B) thickness of the multilayer repeat unit. Each data point is labeled by a (m;n) index for the film where m is the number of Bi_2Te_3 quintet layers and n is the number of $TiTe_2$ sheets in the repeat unit. Also included is the average measured thermal conductivity for the pure $TiTe_2$ samples.

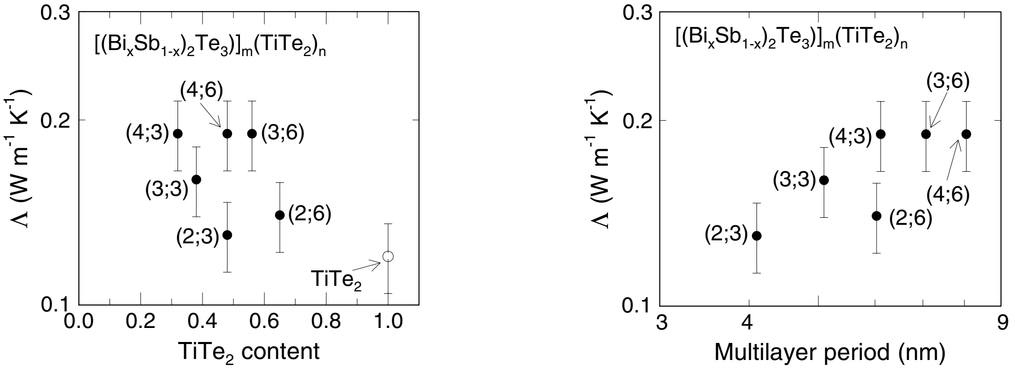

(A) **(B)**

Figure 52. Cross-plane thermal conductivity of $[(Bi_xSb_{1-x})_2Te_3]_m (TiTe_2)_n$ (x = 0.55 +/- 0.09, *m* = 2-4, *n*= 3 and 6) films. Data are plotted as a function of (A) $TiTe_2$ atomic fraction (calculated as $3n/(5m+3n)$); and (B) thickness of the multilayer repeat unit. Each data point is labeled by a (*m*;*n*) index for the film where *m* is the number of $(Bi_xSb_{1-x})_2Te_3$ quintet layers and *n* is the number of $TiTe_2$ sheets in the repeat unit. Also included is the average measured thermal conductivity for the pure $TiTe_2$ samples.

Figure 51 and Figure 52 show the thermal conductivity vs. composition for the superlattice samples. I observed a reduction in the thermal conductivity with increasing $TiTe_2$ content and the values approach that measured for homogenous $TiTe_2$ samples. The thermal conductivity is sensitive to the relative amount of $TiTe_2$ in the sample and not to the density of interfaces or the superlattice period. As described in the previous section, I attribute the low thermal conductivity in the cross-plane direction to strong phonon scattering and anisotropic elastic constants of the turbostratic disordered material, in this case $TiTe_2$. The $(Bi,Sb)_2Te_3$ / $TiTe_2$ multilayer alloy samples have a lower thermal conductivity ($\Lambda_{avg.} = 0.17$ W m^{-1} K^{-1}) than the Bi_2Te_3 / $TiTe_2$ multilayer films ($\Lambda_{avg.} = 0.24$ W m^{-1} K^{-1}) , see Figure 51B and Figure 52B. Compositions that approach pure Bi_2Te_3 have higher thermal conductivity as Bi_2Te_3 does not exhibit turbostratic disorder.

The average thermal conductivity of our homogeneous $TiTe_2$ thin film samples is extremely low, $\Lambda = 0.12$ W m^{-1} K^{-1}. In bulk form, $TiTe_2$ is a semimetal with an electrical conductivity along the *c*-axis that is a factor of 35-40 smaller then the conductivity in the *a-b* plane [90, 91, 92]. The electrical conductivities in the *a-b* plane of our thin film samples are 4100-4600 ohm^{-1} cm^{-1}, a factor of ≈ 2.3 smaller than *a-b* conductivity of bulk90 $TiTe_2$. If the anisotropy of electrical conductivity our thin film samples were the same as in bulk $TiTe_2$, we would expect an electronic contribution to the *c*-axis thermal conductivity of 0.09 W m^{-1} K^{-1}. Given the turbostratic microstructure of our thin film samples, however, I expect that the anisotropy of electrical conductivity will be significantly larger than in the bulk, and the electronic contribution to the *c*-axis thermal conductivity of $TiTe_2$ will be significantly smaller than 0.09 W m^{-1} K^{-1}.

To gain insight into the effect of grain size on the lattice thermal conductivity of Bi_2Te_3, I followed previous work [93] and constructed a Debye-Callaway (D-C) model using the procedure described by Morelli et al. [94]. To constrain the parameters of the D-C model, I estimated the cutoff frequencies ($\theta_L = 96$ K and $\theta_T = 62$ K) by the acoustic phonon frequencies at the zone boundary ($f_L = 2.0\text{x}10^{12}$ Hz; $f_T = 1.3\text{x}10^{12}$ Hz) from calculations of the phonon density of states [95, 96]. I calculate the relative ratio of the anharmonic scattering strengths of umklapp and normal processes, B_U and B_N, using equations 10 and 25 (with $a = 2$, $b = 1$) from Reference 94: $B_U = \hbar \gamma^2 / (M v^2 \theta)$ and $B_N = k_B \gamma^2 V^{1/3} / (M v^3)$ for the longitudinal and transversal propagation modes. Here $\hbar$ is the reduced Planck constant, k_B is the Boltzmann constant, $\gamma_L = 1.0$ and $\gamma_T = 0.7$ are the mode Grüneisen constants, $M = 2.66\text{x}10^{-25}$ kg and $V = 3.38\text{x}10^{-29}$ m^3 are the average mass and volume per atom, v is the speed of sound and θ is the cutoff frequency. Phonon scattering by isotope disorder calculated with equation 16 of Reference 94 is negligible ($\Gamma = 8.21\text{x}10^{-5}$). A boundary scattering rate $\tau^{-1} = v / h$ describes phonon scattering by grain boundaries and hetero-interfaces; v is the speed of sound and h is the grain size. I estimated the polycrystalline average rigidity modulus G and bulk modulus K from elastic properties [89] of single crystal Bi_2Te_3 using the Voigt-Reuss-Hill method [97, 98] , i.e., the arithmetic mean of G and K moduli calculated by the Voigt and Reuss approaches. I calculated the transversal and longitudinal polycrystalline average speeds of sound as $v_T = \sqrt{G/\rho}$ = 1590 m/s and $v_L = \sqrt{(K + 4G/3)/\rho}$ =2840 m/s, where ρ = 7.86 g/cm^3 is the mass density of Bi_2Te_3.

Our implementation of the D-C model does not include heat transport by optical phonons and, because of the relatively low cut-off frequencies for the acoustic branches, greatly restricts the number of acoustic phonons that contribute to heat transport in the model; in fact, <10% of the 3N vibrational modes of the crystal are included in this approach. To account for heat transport by phonons that are neglected by the model, I estimate the thermal conductivity of these phonons using the calculated minimum thermal conductivity Λ_{min} of Bi_2Te_3.

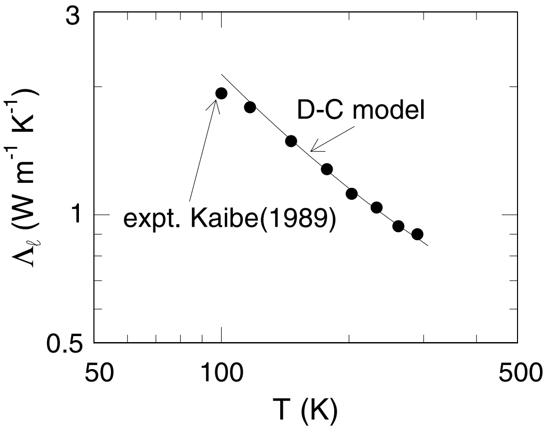

Figure 53. Plot of experimental lattice thermal conductivity of single crystal Bi_2Te_3 (Reference 99, filled circles) fitted with predictions of the Debye-Callaway (D-C) model described in the study (solid line).

To fit the strength of anharmonic phonon scattering in the D-C model, the calculations of the D-C model are added to the minimum thermal conductivity, Λ_{min} =0.31 W m^{-1} K^{-1}, and then compared to data for bulk [99] Bi_2Te_3, see Figure 53. For the calculations, I vary the coefficients B_U and B_N while keeping their relative ratio fixed and set the grain size of the sample to a large value *h*= 4 mm (i.e., single crystal sample). The values I obtained thus are: B_{UL} = 9.7x10^{-18} s K^{-1}, B_{UT} = 23x10^{-18} s K^{-1}; B_{NL} = 14x10^{-18} s K^{-1}, B_{NT} = 39x10^{-18} s K^{-1}.

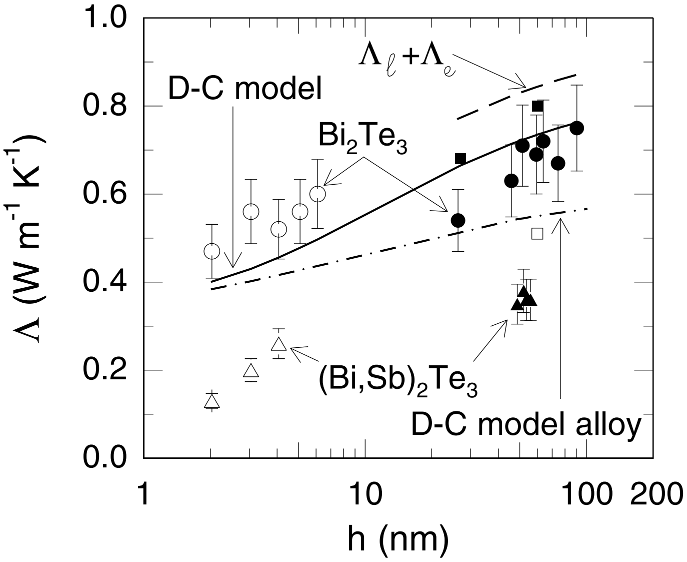

Figure 54. Thermal conductivity Λ measured for homogeneous Bi_2Te_3 (full circles) and $(Bi,Sb)_2Te_3$ alloy (full triangles) plotted as a function of grain size or layer thickness *h*. Also included are literature values for small grain polycrystalline Bi_2Te_3 samples (References 100 – open square and 101 – filled squares). The open circles and triangles represent effective Λ for Bi_2Te_3 and respectively $(Bi,Sb)_2Te_3$ alloy layers calculated from measured Λ of multilayer $[(Bi_2Te_3)_m(TiTe_2)_n]$ (Figure 51B) and $[(Bi_xSb_{1-x})_2Te_3]_m (TiTe_2)_n$ (Figure 52B) films. The solid line is the D-C model calculation of lattice thermal conductivity of Bi_2Te_3 with the assumption of a boundary scattering length that is equal to the thickness of the sample. Minimum thermal conductivity of Bi_2Te_3 is added in the model calculation to account for heat transport by high frequency acoustic and optical phonons. The dashed line represents the calculated total thermal conductivity of Bi_2Te_3 with contributions from D-C model and the electronic thermal conductivity. The dash-dot line is the D-C model calculation of lattice thermal conductivity of $(Bi,Sb)_2Te_3$ alloy with the addition of strong point-defect phonon scattering, Γ=0.3.

In Figure 54, I compare the thermal conductivity Λ measured for the various Bi_2Te_3 layers to the predictions of the D-C model as a function of grain size. This plot includes data for homogeneous, nanocrystalline Bi_2Te_3 that I previously presented as a function of annealing temperature; see Figure 48 and Figure 49. For comparison, I included in Figure 54 examples of other previous work [100, 101] on small grain Bi_2Te_3.

To extract the effective thermal conductivity of the nanoscale Bi_2Te_3 layers in the multilayer $[(Bi_2Te_3)_m(TiTe_2)_n]$ samples, see Figure 51B, I ignore possible contributions to the thermal resistance from the $Bi_2Te_3/TiTe_2$ interfaces and apply a simple effective medium model that treats the thermal resistance of the multilayer as the sum of the thermal resistances of the individual layers; i.e., I solve for the thermal conductivity of the Bi_2Te_3 layers Λ-Bi_2Te_3 in equation:

$$\frac{x+y}{\Lambda - multilayer} = \frac{x}{\Lambda - Bi_2Te_3} + \frac{y}{\Lambda - TiTe_2}, \tag{4}$$

where x and y are the individual layer thicknesses in the multilayer repeat period and Λ-$TiTe_2$= 0.12 W m^{-1} K^{-1}.

The Bi_2Te_3 data closely follow the trend in the lattice thermal conductivity predicted by the D-C model. As the grain size is reduced toward 2 nm, the lattice thermal conductivity approaches the lower limit predicted by the model of the minimum thermal conductivity, 0.31 W m^{-1} K^{-1}. Similar values are observed [87] in short period superlattices of Bi_2Te_3/Sb_2Te_3. For grain sizes on the order of ~50 nm, my data and modeling indicate that the reduction in thermal conductivity compared to the reported bulk values [99] is observable but small, ≈ 13%. This conclusion was also reached by

Shi [102, 103] and co-workers from their studies of the thermal conductivity of 50 nm diameter Bi_2Te_3 nanowires.

I emphasize that my measurements are for the total thermal conductivity but the D-C model does not include the electronic contribution. I estimate the electronic contribution to the thermal conductivity of the nanocrystalline films from measurements of the in-plane electrical conductivity of Bi_2Te_3 films deposited on fused-quartz substrates using the same recipe as the films that were deposited on Si for the thermal conductivity measurements. (TDTR measurements require high thermal conductivity substrates.) Electrical measurements in the *a-b* plane showed the films are *n*-type Bi_2Te_3; Seebeck coefficient and electrical conductivity varied with increasing annealing time from -83 to -137 μV/K and 436 to 1482 (ohm-cm)$^{-1}$, respectively. I estimate the electronic component of the thermal conductivity Λ_e using the Wiedemann Franz law with a non-degenerate Lorenz number $L = 2(k_B/e)^2 = 1.45\times10^{-8}$ V^2/K^2 and electrical conductivity equal to ¼ the average of the *a-b* plane values [104, 105] . I add the result, $\Lambda_e \approx 0.11$ W m^{-1} K^{-1} to the D-C model and plot the sum as the dashed line in Figure 54. The data fall below this curve indicating either that the anisotropy in electrical conductivity is greater than a factor of 4 or that the D-C model overestimates the lattice thermal conductivity of our nanocrystalline Bi_2Te_3 films.

Figure 54 also summarizes the measurements of the thermal conductivity of $(Bi,Sb)_2Te_3$ layers as a function of grain size. As before, I extracted the effective thermal conductivity of nanoscale $(Bi,Sb)_2Te_3$ layers from measurements on multilayer $[(Bi,Sb)_2Te_3]_m(TiTe_2)_n$ films (Figure 52B) using an effective medium model and the measured thermal conductivity of $TiTe_2$:

$$\frac{x+y}{\Lambda - multilayer} = \frac{x}{\Lambda - (Bi,Sb)_2Te_3} + \frac{y}{\Lambda - TiTe_2}\,. \tag{5}$$

Average measured thermal conductivity of the $(Bi_{0.5}Sb_{0.5})_2Te_3$ films is 0.36 W m^{-1} K^{-1}, a factor of 1.9 smaller than that of homogeneous Bi_2Te_3 layers with similar grain size. Electrical measurements in the *a-b* plane of the $(Bi_{0.5}Sb_{0.5})_2Te_3$ films deposited on fused-quartz substrates indicate *n*-type conduction: Seebeck coefficient and electrical conductivity varied with increasing annealing time from -23 to -113 μV/K and 109 to 211 $(\text{ohm-cm})^{-1}$, respectively. As before, I estimate the electronic component of the thermal conductivity using the Wiedemann-Franz law with a non-degenerate Lorenz number and electrical conductivity equal to 1/4 the average of the *a-b* plane values [106], $\Lambda_e = 0.02$ W m^{-1} K^{-1}. The average lattice thermal conductivity obtained by subtracting the small electronic component from the measured thermal conductivity is a factor of ≈ 2 smaller than the lattice thermal conductivity of Bi_2Te_3 layers predicted by the D-C model. The magnitude of this reduction is comparable to what is observed in bulk $(Bi,Sb)_2Te_3$ alloys [107, 108]. These observations are confirmed by recent reports on p-type $Bi_{0.5}Sb_{1.5}Te_3$ nanocrystalline bulk alloys [109, 110] that estimate lattice thermal conductivity ≈ 0.3 W m^{-1} K^{-1} in the limit of low grain size (d<10 nm).

The reduction in lattice thermal conductivity of $(Bi,Sb)_2Te_3$ alloys is typically attributed to phonon Rayleigh scattering created by variations in atomic mass and chemical bonding when Bi atoms are replaced by Sb. Calculations of point defect scattering by mass disorder are relatively straightforward but scattering rates created by variations in bond-length or bond-strength disorder are difficult to estimate; furthermore, even if the cross sections could be estimated, I do not know if the total cross sections for the variations scattering terms (mass, bond-length, bond-strength) should be added or if interference between the various scattering terms needs to be taken into account. Therefore, to gain insight in the magnitude of the reduction in thermal conductivity that might be created by point defect scattering in a $(Bi,Sb)_2Te_3$ alloy, I added to the D-C model what I believe is a reasonable upper limit to the point defect scattering rate [111, 112] , $\Gamma=0.3$. The result is included in Figure 54. In this calculation, the lattice thermal conductivity is suppressed by a factor of 1.3 for grain sizes $d \approx 50$ nm; adding point defect scattering to the model has little effect in the limit of small grain size, $d<10$ nm, where the thermal conductivity has already been reduced close to the minimum value.

Data for the alloy layers, however, fall significantly below the calculation in the limit of small grain size and therefore also fall well below the prediction of the model of the minimum thermal conductivity. It is not yet clear the difference in conductivity between Bi_2Te_3 and $(Bi,Sb)_2Te_3$ alloy layers at small grain sizes, $d<10$ nm, where the effects of point defect scattering should be small; I can only speculate at this time that the effective thermal conductivities of the $(Bi,Sb)_2Te_3$ layers in the alloy multilayers $[(Bi,Sb)_2Te_3]_m(TiTe_2)_n$ are being suppressed by the effects of interface resistance that are stronger in the alloy multilayers than in the $(Bi_2Te_3)_m(TiTe_2)_n$ multilayers.

5.4 Conclusions

Multilayer films incorporating turbostratic $TiTe_2$ enable studies of the effective thermal conductivity of Bi_2Te_3 layers as thin as 2 nm. In the limit of small grain size or layer thickness, the thermal conductivity of Bi_2Te_3 approaches the predicted minimum thermal conductivity of 0.31 W m^{-1} K^{-1}. The dependence of the thermal conductivity on grain size is in good agreement with the Debye-Callaway model for a range of grain sizes

1-100 nm. Very low thermal conductivities ($\Lambda = 0.20$ W m^{-1} K^{-1}) can be achieved by combining the effects of alloying and turbostratic disorder in a multilayer structure.

REFERENCES

1 J. Callaway, Phys. Rev. **113**, 1046 (1959).

2 M. G. Holland, Phys. Rev. **132**, 2461 (1963).

3 A. Einstein, Ann. Phys. **35**, 679 (1911).

4 D. G. Cahill, S. K. Watson, R. O. Pohl, Phys. Rev. B **46**, 6131 (1992).

5 R. M. Costescu, D. G. Cahill, F. H. Fabreguette, Z. A. Sechrist, S. M. George, Science **303**, 989 (2004).

6 Y. S. Ju, M.-T. Hung, M. J. Carey, M.-C. Cyrille, J. R. Childress, Appl. Phys. Lett. **86**, 203113 (2005).

7 E. T. Schwartz and R. O. Pohl, Rev. Mod. Phys. **61**, 605 (1989).

8 C. A. Paddock, G. L. Eesley, J. Appl. Phys. **60**, 285 (1986).

9 D. A. Young, C. Thomsen, H. T. Grahn, H. J. Maris, and J. Tauc, in “Phonon Scattering in Condensed Matter”, edited by A. C. Anderson and J. P. Wolfe (Springer, Berlin, 1986), p. 49.

10 D. G. Cahill, Rev. Sci. Instrum. **75**, 5119 (2004).

11 D. G. Cahill, K. E. Goodson, and A. Majumdar, J. Heat Transfer **124**, 223 (2002).

12 D. G. Cahill, W. K. Ford, K. E. Goodson, G. D. Mahan, A. Majumdar, H. J. Maris, R. Merlin, and S. R. Phillpot, J. Appl. Phys. **93**, 793 (2003).

13 R. B. Schwarz, W. L. Johnson, Phys. Rev. Lett. **51**, 415 (1983).

14 M. Noh, J. Theil and D. C. Johnson, Science **270**, 1181 (1995).

15 F. R. Harris, S. Standridge and D. C. Johnson, J. Amer. Chem. Soc. **127**, 7843 (2005).

16 M. Noh, C. D. Johnson, M. D. Hornbostel, J. Thiel, and D. C. Johnson, Chem. Mater. **8**, 1625 (1996).

17 Q. Lin, C. L. Heideman, N. Nguyen, P. Zschack, C. Chiritescu, D. G. Cahill, D. C. Johnson, Eur. J. Inorg. Chem. **15**, 2382 (2008)

18 “Physics And Chemistry Of Materials With Layered Structures”, Volumes 1 - 6, (D. Reidel Pub. Co., Boston).

19 J. A. Wilson, A. D. Yoffe, Adv. Phys. **18**, 193 (1969)

20 L. Fister, X.-M. Li, J. McConnell, T. Novet, and D. C. Johnson, J. Vac. Sci. Technol. **11**, 3014 (1993).

21 V. D. Scott, G. Love and S. J. B. Reed, “Quantitative Electron-Probe Microanalysis”, 2nd edition, (Prentice Hall, 1995).

22 STRATAGem 3.0 Thickness and Compositional Thin Film Analysis Package, (SAMx, Saint Andre de la Roche, France, 1997).

23 L. C. Feldman and J. W. Mayer, “Fundamentals of Surface and Thin Film Analysis”, (North Holland-Elsevier, New York, New York, 1986), p. 39.

24 M. Mayer, SIMNRA User’s Guide, Report IPP 9/113, Max-Planck-Institut für Plasmaphysik, Garching, Germany, 1997.

25 W. K. Chu, J. W. Mayer and M. A. Nicolet, “Backscattering Spectrometry”, (Academic Press, New York, 1978).

26 K. Kang, Y. K. Koh, C. Chiritescu, X. Zheng, and D. G. Cahill, Rev. Sci. Instrum. **79**, 114901 (2008).

27 R. M. Costescu, M. A. Wall, and D. G. Cahill, Phys. Rev. B **67**, 54302 (2003).

28 W. S. Capinski, H. J. Maria, T. Ruf, M. Cardona, K. Ploog, and D. S. Katzer, Phys. Rev. B **59**, 8105 (1999).

29 V. K. Pecharsky and P. Y. Zavalij, "Fundamentals of powder diffraction and structural characterization of materials" (Springer, New York, 2003), p.137.

30 P. D. Desai, H. M. James, C. Y. Ho, J. Phys. Chem. Ref. Data **13**, 1131 (1984).

31 D. A. Ditmars, C. A. Plint, and R. C. Shukla, Int. J. Thermophys. **6**, 499(1985).

32 P. D. Desai, J. Phys. Chem. Ref. Data **15**, 967 (1986).

33 W. Fulkerson, J. P. Moore, R. K. Williams, R.S. Graves, D.L. McElroy, Phys. Rev. **67**, 765 (1968).

34 Y. S. Touloukian and E. H. Buyco, eds., Thermophysical Properties of Matter, vol. 5 (IFI/Plenum, New York-Washington, 1970).

35 N P Gorbachuk, A S Bolgar, V R Sidorko, and L V Goncharuk, Powder Metall. Met. Ceram. **43**, 284 (2004).

36 V M Zhdanov, Russian J. Phys. Chem. **45**, 1357 (1971).

37 N. V. Baranov, V. G. Pleshchev, N. V. Selezneva, E. M. Sherokalova, A. V. Korolev, V. A. Kazantsev and A. V. Proshkin, J. Phys.: Condens. Matter **21**, 506002 (2009).

38 A. S. Bolgar, Zh. A. Trofimova, A. A. Yanaki, Powder Metall. Met. Ceram. **29**, 382 (1990).

39 H. L. Kiwia and E. F. Westrum, Jr., J. Chem. Thermodynamics **7**, 683(1975).

40 A. V. Blinder, A. S. Bolgar and Zh. A. Trofimova, Powder Metall. Met. Ceram. **32**, 234 (2004).

41 D. H. Parkinson and J. E. Quarrington, Proc. Phys. Soc. A **67**, 569 (1954).

42 E. P. Donovan, F. Spaepen, D. Turnbull, J. M. Poate, and D. C. Jacobson, Appl. Phys. Lett. **42**, 698 (1983).

43 E. P. Donovan. F. Spaepen. D. Turnbull. J. M. Poate, and D. C. Jacobson, J. Appl. Phys. **57**, 1795 (1985).

44 K. H. Tsang, H. W. Kui, and K. P. Chik, J. Appl. Phys. **74**, 4932 (1993).

45 D. G. Cahill and F. Watanabe, Phys. Rev. B **70**, 235322 (2004).

46 J.-C. Zhao, X. Zheng and D. G. Cahill, Materials Today **10**, 28 (2005)

47 D. G. Cahill, Rev. Sci. Instrum. **61**, 802 (1990).

48 D. G. Cahill, M. Katiyar, and J. R. Abelson, Phys. Rev. B **50**, 6077 (1994).

49 B. C. Gundrum, D. G. Cahill, R. S. Averback, Phys. Rev. B **72**, 245426 (2005).

50 E. Lopez-Honorato, C. Chiritescu, P. Xiao, D. G. Cahill, G. Marsh, and T. J. Abram, J. Nucl. Mater. **378**, 35 (2008).

51 S. Huxtable, D. G. Cahill, V. Fauconnier, J. O. White and J–C Zhao, Natur. Mater. **3**, 298 (2004).

52 C. Thomsen, H. T. Grahn, H. J. Maris, and J. Tauc, Phys. Rev. B **34**, 4129 (1986).

53 K. E. O'Hara, X. Hu, and D. G. Cahill, J. Appl. Phys. **90**, 4852 (2001).

54 C. Thomsen, H. T. Grahn, H. J. Maris, and J. Tauc, Opt. Commun. **60**, 55 (1986).

55 CRC Handbook of Chemistry and Physics, 87th Edition, David R. Lide, ed., (Taylor and Francis, Boca Raton, FL, 2007).

56 H. J. McSkimin, J. Appl. Phys. **24**, 988 (1953).

57 P. B. Allen, J. L. Feldman, Phys. Rev. B **48**, 12581 (1993).

58 R. M. Costescu, D. G. Cahill, F. H. Fabreguette, Z. A. Sechrist, S. M. George, Science **303**, 989 (2004).

59 Y. S. Ju, M.-T. Hung, M. J. Carey, M.-C. Cyrille, J. R. Childress, Appl. Phys. Lett. **86**, 203113 (2005).

60 A. P. Hammersley, FSRF Internal Report No. EXP/AH/93-02, FIT2D Reference Manual (1993). Available at http://www.esrf.eu/computing/scientific/FIT2D/

61 J.F. Ziegler, SRIM 2003. Available from <www.srim.org>.

62 G. Muller and S. Kalbitzer, Philos. Mag. B **41**, 307 (1980).

63 D. E. Moncton, J. D. Axe, and F. J. DiSalvo, Phys. Rev. B **16**, 801 (1977).

64 P. A. Medwick and R. O. Pohl, J. Solid State Chem. **133**, 44 (1997).

65 J. Edwards and R. F. Frindt, J. Phys. Chem. Solids **32**, 2217 (1971).

66 H. N. S. Lee, H. McKinzie, D. S. Tannhauser and A. Wold, J. Appl. Phys. 40, 602, 1969.

67 S.-M. Lee, D. G. Cahill, and R. Venkatasubramanian, Appl. Phys. Lett. **70**, 2957 (1997).

68 M. H. Van Maaren, Phys. Lett. A **40**, 353 (1972).

69 L. Otero-Diaz, J. D. FitzGerald, T. B. Williams, and B. G. Hyde, Acta Crystallogr. B **41**, 405 (1985).

70 G. A. Wiegers and A. Meerschaut, Mater. Sci. Forum **100-101**, 101 (1992).

71 S. Van Smaalen, A. Meetsma, G. A. Wiegers, and J. L. De Boer, Acta Crystallogr. B **47**, 314 (1991).

72 A. Meerschaut, Y. Moelo, L. Cario, A. Lafond, and C. Deudon, Mol. Cryst. Liq. Cryst. **341**, 1 (2000).

73 U. Pietsch, V. Holy, and T. Baumbach, “High resolution x-ray scattering”, (Springer, New York, 2004).

74 G. Lippmann, P. Kastner and W. Wanninger, Phys. Status Solidi A **6**, K159 (1971).

75 L. Hu, P. Keblinski, S. Shenogin, and D. G. Cahill, “Origin of ultra-low thermal conductivity in disordered, layered crystals”, submitted for publication.

76 H. Scherrer and S. Scherrer in “Thermoelectrics Handbook: Macro to Nano”, edited by D. M. Rowe (CRC Press, Boca Raton, Florida, 2006), chapter 27.

77 B. Poudel, Q. Hao, Y. Ma, Y. Lan, A. Minnich, B. Yu, X. Yan, D. Wang, A. Muto, D. Vashaee, X. Chen, J. Liu, M. S. Dresselhaus, G. Chen, and Z. Ren, Science **320**, 634 (2008).

78 L.-D. Zhao, B.-P. Zhang; W.-S. Liu, and J.-F. Li, J. Appl. Phys. **105**, 023704 (2009).

79 J. O. Barnes, J. A. Rayne and R. W. Ure Jr., Phys. Lett. A **46**, 317 (1974).

80 T. L. Anderson and H. B. Krause, Acta Cryst. B **30**, 1307 (1974).

81 O. Madelung, ed., “Non-Tetrahedrally Bonded Elements and Binary Compounds I”, Landolt-Börnstein series, Vol. III / 41C (Springer-Verlag, Berlin, 1998).

82 B. -L. Huang and M. Kaviany, Phys. Rev. B **77**, 125209 (2008).

83 Z. Hurych and R. L. Benbow, Phys. Rev. B **16**, 3707 (1977).

84 Y. Arnaud and M. Chevreton, J. Solid State Chem. **39**, 230 (1981).

85 M. Scharli and F. Lévy, Phys. Rev. B **33**, 4317 (1986).

86 W. G. Stirling, B. Dorner, J. D. N. Cheeke, and J Revelli, Solid State Comm. **18**, 931 (1976).

87 M. N. Touzelbaev, P. Zhou, R. Venkatasubramanian and K. E. Goodson, J. Appl. Phys. **90**, 763 (2001)

88 O. Madelung, ed., “Numerical Data and Functional Relationships in Science and Technology, New Series”, Landolt-Bornstein series, volumes III-17f and III-29a, (Springer-Verlag, Berlin, 1998)

89 J. O. Jenkins, J. A. Rayne, and R. W. Ure, Phys. Rev. B **5**, 3171 (1972); 6, 1609 (1972).

90 P. B. Allen and N. Chetty, Phys. Rev. B **50**, 14855 (1994).

91 L Perfetti, C. Rojas, A. Reginelli, L. Gavioli, H. Berger, G. Margaritondo, M. Grioni, R. Gaal, L. Forro, and F. R. Albenque, Phys. Rev. B **64**, 115102 (2001).

92 D. K. G. de Boer, C. F. van Bruggen, G. W. Bus, R. Coehoorn, C. Hass, G. A. Sawatzky, H. W. Myron, D. Norman, and H. Padmore, Phys. Rev. B **29**, 6797 (1984).

93 Y. K. Koh and D. G. Cahill, Phys. Rev. B **76**, 075207 (2007).

94 D. T. Morelli, J. P. Heremans and G. A. Slack, Phys. Rev. B **66**, 195304 (2002).

95 B. -L. Huang and M. Kaviany, Phys. Rev. B **77**, 125209 (2008).

96 V. Wagner, G. Dolling, B. M. Powell and G. Landwehr, Phys. Stat. Sol. (B) **85**, 311 (1978).

97 R. Hill, Proc. Phys. Soc. A **65**, 349 (1952).

98 O. L. Anderson, J. Phys. Chem. Solids **24**, 909 (1963).

99 H. Kaibe, Y. Tanaka, M. Sakata and I. Nishida, J. Phys. Chem. Solids **50**, 945 (1989)

100 M. R. Dirmyer, J. Martin, G. S. Nolas, A. Sen, and J. V. Badding, Small **5**, 933 (2009).

101 M. Takashiri, K. Miyazaki, S. Tanaka, J. Kurosaki, D. Nagai, and H. Tsukamoto, J. Appl. Phys. **104**, 084302 (2008).

102 A. Mavrokefalos, A. L. Moore, M. T. Pettes, L. Shi, W. Wang and X. G. Li, J. Appl. Phys. **105**, 104318 (2009).

103 J. H. Zhou, Q. Jin, J. H. Seol, X. Li, and L. Shi, Appl. Phys. Lett. **87**, 133109 (2005)

104 R. T. Delves, A. E. Bowley, D. W. Hazelden and H. J. Goldsmid, J. Proc. Phys. Soc. **78**, 838 (1961)

105 J. R. Drabble, Proc. Phys. Soc. Lond. **71**, 730 (1957).

106 T. Caillat, M. Carle, P. Pierrat, H. Scherrer and S. Scherrer, J. Phys. Chem. Solids **53**, 1121 (1992).

107 K. Yokota and S. Katayama, Jpn. J. Appl. Phys. **12**, 1205 (1973).

108 W. M. Yim and F. D. Rosi, Solid-State Electron. **15**, 1121 (1972).

109 Y. Ma, Q. Hao, B. Poudel, Y. Lan, B. Yu, D. Wang, G. Chen, and Z. Ren, Nano Lett. **8**, 2580 (2008).

110 W. Xie, X. Tang, Y. Yan, Q. Zhang, and T. M. Tritt, J. Appl. Phys. **105**, 113713 (2009).

111 Y. K. Koh, C. J. Vineis, S. D. Calawa, M. P. Walsh, and D. G. Cahill, Appl. Phys. Lett. **94**, 153101 (2009).

112 B. Abeles, Phys. Rev. **131**, 1906 (1963).